

Review Article

Progress in Dual (Piezoelectric-Magnetostrictive) Phase Magnetoelectric Sintered Composites

Rashed Adnan Islam¹ and Shashank Priya²

¹ Philips Lumileds Lighting Co., 370 W. Trimble Road, San Jose, CA 95131, USA

² Materials Science and Engineering, Virginia Tech, Blacksburg, VA 24061, USA

Correspondence should be addressed to Rashed Adnan Islam, rashed_ms@yahoo.com

Received 26 September 2011; Accepted 2 December 2011

Academic Editor: Vladimir Petrov

Copyright © 2012 R. Adnan Islam and S. Priya. This is an open access article distributed under the Creative Commons Attribution License, which permits unrestricted use, distribution, and reproduction in any medium, provided the original work is properly cited.

The primary aims of this review article are (a) to develop the fundamental understanding of ME behavior in perovskite piezoelectric-spinel magnetostrictive composite systems, (b) to identify the role of composition, microstructural variables, phase transformations, composite geometry, and postsintering heat treatment on ME coefficient, and (c) to synthesize, characterize, and utilize the high ME coefficient composite. The desired range of ME coefficient in the sintered composite is 0.5–1 V/cm·Oe. The studies showed that the soft piezoelectric phase quantified by smaller elastic modulus, large grain size of piezoelectric phase (~1 μm), and layered structures yields higher magnitude of ME coefficient. It is also found that postsintering thermal treatment such as annealing and aging alters the magnitude of magnetization providing an increase in the magnitude of ME coefficient. A trilayer composite was synthesized using pressure-assisted sintering with soft phase [0.9 PZT–0.1 PZN] having grain size larger than 1 μm and soft ferromagnetic phase of composition Ni_{0.8}Cu_{0.2}Zn_{0.2}Fe₂O₄ [NCZF]. The composite showed a high ME coefficient of 412 and 494 mV/cm·Oe after sintering and annealing, respectively. Optimized ferrite to PZT thickness ratio was found to be 5.33, providing ME coefficient of 525 mV/cm·Oe. The ME coefficient exhibited orientation dependence with respect to applied magnetic field. Multilayering the PZT layer increased the magnitude of ME coefficient to 782 mV/cm·Oe. Piezoelectric grain texturing and nanoparticulate assembly techniques were incorporated with the layered geometry. It was found that with moderate texturing, d_{33} and ME coefficient reached up to 325 pC/N and 878 mV/cm·Oe, respectively. Nanoparticulate core shell assembly shows the promise for achieving large ME coefficient in the sintered composites. A systematic relationship between composition, microstructure, geometry, and properties is presented which will lead to development of high-performance magnetoelectric materials.

1. Magnetoelectric Effect

The coexistence of coupled electrical and magnetic properties in the “magnetoelectric” material has led to the possibility of developing smarter and smaller electronic components. In order to make this possibility a reality, significant efforts are required to understand the science of magnetoelectric (ME) behavior and apply this understanding to develop higher sensitivity material. The primary aim of this review is to identify the role of composition, microstructural variables, composite geometry, texturing, postsintering heat treatment, and nanoscale assembly on ME coefficient. The overall objective is to analyze the synthesis process and properties and provide new applications for ME composite.

Magnetoelectric effect is the combination of two types of materials property such as magnetostriction and piezoelectricity [1–3]. Magnetoelectric effect can be described as the induced electrical polarization under magnetic field or induced magnetization under electric field. Under applied alternating magnetic field, the magnetostrictive phase produces strain which is transferred on to the piezoelectric phase that converts strain into electric charge. On the other hand, under applied electric field, piezoelectric phase produces strain which is transferred on to the magnetostrictive phase that converts it into magnetic field. The former is called the direct magnetoelectric effect and the later is called the converse magnetoelectric effect [4, 5]. These materials are extremely promising for applications

such as sensors, actuator, transducer, storage devices, and various other applications [6–8]. The interrelation between ferroelectricity and magnetism allows the magnetic control of ferroelectric properties and vice versa [9–12]. Figure 1 shows the interrelation between electric field, magnetic field, and stress. A ferromagnetic and ferroelectric phase can be combined in several different ways, including naturally occurring composites, artificially designed composites, and *in-situ* sintered composites [13, 14].

2. Thermodynamic Considerations of Magnetolectricity

The thermodynamic consideration of magnetolectric effect is obtained from the expansion of free energy of the system in terms of magnetic and electric field, such as

$$G(\vec{E}, \vec{H}) = G_0 - P_s \vec{E} - M_s \vec{H} - \frac{1}{2} \chi_{ij}(E) E_i E_j - \frac{1}{2} \chi_{ij}(H) H_i H_j - \alpha_{ij} \vec{E}_i \vec{H}_j, \quad (1)$$

where \vec{E} and \vec{H} are the electric field and magnetic field, respectively [15]. Differentiation of (1) gives us polarization and magnetization as follows:

$$P_i = - \left(\frac{\delta G}{\delta E} \right) = P_s + \chi_{ij} E_j + \alpha_{ij} H_j, \quad (2)$$

$$M_i = - \left(\frac{\delta G}{\delta H} \right) = M_s + \chi_{ij} H_j + \alpha_{ij}. \quad (3)$$

Here, α_{ij} is the magnetolectric tensor. Magnetolectric effect combines two important materials property, permittivity, and permeability, and for a single phase material, they define the upper limit of α_{ij} as follows [15]:

$$\alpha_{ij} < \sqrt{\varepsilon_{ij} \mu_{ij}}. \quad (4)$$

Many of the single-phase materials posses either low permittivity or low permeability or both, as a consequence of which the magnetolectric coupling is small. For magnetolectric composite materials, an indirect coupling between ferroelectric and ferromagnetic phase can be established via strain. Piezoelectricity defines the materials property that converts applied stress into proportional electric charge. The linear constitutive equations for a piezoelectric material are given as

$$D_3 = \varepsilon_{33}^T E_3 + d_{33} T_3, \quad (5)$$

$$S_3 = d_{33} E_3 + s_{33}^E T_3, \quad (6)$$

where D , E , T , and S are the dielectric displacement, electric field, stress, and strain, ε is the permittivity, s is elastic compliance, and d is piezoelectric charge constant. The constitutive equations for magnetostriction are given as [16]

$$S = s^H T + q H, \quad (7)$$

$$B = q T + \mu^T H, \quad (8)$$

where B , q , μ , and H are magnetic induction, piezo magnetic coefficient, permeability, and magnetic field. Magnetolectric coefficient of a composite can be described in direct notation of tensors as

$$T = cS - e^T E - \alpha S^m, \quad (9)$$

$$D = eS + \varepsilon E + \alpha H, \quad (10)$$

$$B = \mu(\varepsilon, E, H)H, \quad (11)$$

where σ , ε , D , E , B , H , c , and K are the stress, strain, electric displacement, electric field, magnetic induction, magnetic field, stiffness constant at constant field, and dielectric constant at constant strain and magnetic field, respectively [17]. The models proposed in literature show variation of ME coefficient with piezoelectric coefficient, piezomagnetic coefficient, and elastic compliances of piezoelectric and magnetostrictive phases. Srinivasan et al. have proposed the ME coefficient as

$$\frac{\delta E_3}{\delta H_1} = \frac{-2d_{31}^p q_{11}^m v^m}{(s_{11}^m + s_{12}^m) \varepsilon_{33}^{T,P} v^p + (s_{11}^p + s_{12}^p) \varepsilon_{33}^{T,P} v^m - 2(d_{31}^p)^2 v_m^m}, \quad (12)$$

where d_{31}^p is the piezoelectric coefficient, v^m and v^p are the volume of magnetic and piezoelectric phase, t^m and t^p are the thickness of magnetic and piezoelectric phase, s_{11}^p , s_{12}^p are the elastic compliances for piezoelectric phase, s_{11}^m , s_{12}^m are the elastic compliances for magnetostrictive phase, q_{11} is the piezomagnetic coefficient of the magnetic phase, and $\varepsilon_{33}^{T,P}$ is the permittivity of the piezoelectric phase. Dong et al. have derived the expression for the magnetolectric coefficient in T-T mode as

$$\left| \frac{dV}{dH} \right|_{T-T} = \beta \frac{n(1-n) A d_{33,m} d_{31,p} g_{31,p}}{S_{11}^E [n S_{11}^E (1 - k_{31}^2) + (1-n) S_{11}^H]}, \quad (13)$$

where β is a constant related to DC magnetic field with a maximum value of 1, n is the thickness ratio of magnetostrictive layer to composite thickness, d is the piezoelectric strain constant, s is the elastic constant, g is the piezoelectric voltage constant, A is the cross-sectional area of the laminate, and k is the electromechanical coupling factor. The relevance of the constant β was not explained in this model. Clearly, the ME coefficient is directly related to piezoelectric constant which is related to dielectric permittivity [$d_{31}^2 = k_{31}^2 (s_{11}^E \varepsilon_{33}^T)$] and piezomagnetic coefficient which is related to permeability [$q_{11,m} = \mu_{33} \cdot s_{33} \cdot \lambda_{33}$].

3. Magnetolectric Single Phase Materials

The history of the magnetolectric effect dates back to 1894 when Pierre Curie observed that a body with asymmetric molecules gets electrically polarized under magnetic field and vice versa. In 1958, Landau and Lifshitz conducted the feasibility study on the presence of magnetolectric

effect in crystals of specific symmetry. Later Dzyaloshinskii showed the violation of time-reversal symmetry explicitly for a single-phase antiferromagnetic system (Cr_2O_3). In 1960, Astrov presented the experimental evidence of ME effect in Cr_2O_3 in a wide temperature range of 80–330 K [18, 19]. Smolensky and Ioffe synthesized the antiferromagnetic ferroelectric perovskite ceramic $\text{Pb}(\text{Fe}_{1/2}\text{Nb}_{1/2})\text{O}_3$ (PFN). Later, single crystals of PFN were grown and the presence of weak spontaneous magnetic moment in the ferroelectric phase below 9 K was confirmed [20]. Recently, single-phase thin-film multiferroic systems, such as perovskite type BiFeO_3 or BiMnO_3 , the boracite family, BaMF_4 families where M is the divalent transition metal, hexagonal RMnO_3 where R is rare earth metals, are of interest to understand the magnetoelectric coupling between two types of dipoles [21–24]. These single-phase materials show two transitions, one corresponding to paraelectric to ferroelectric phase and another corresponding to ferro/ferri/antiferromagnetic to paramagnetic phase. The mechanism for the observance of magnetoelectric effect in single-phase materials is specific to a family. For example—stereochemical activity of Bi lone pair for BiFeO_3 , frustrated spin resulting from magnetoelastic lattice modulations for TbMnO_3 , and charge ordering in doped perovskite [14]. Single-phase magnetoelectric (ME) materials suffer from the drawback that the ME effect is considerably weak. They can be used only at very low temperature and involve expensive materials and processing technique, and they have disadvantage of degradation under cyclic conditions. The reason behind this is that the single-phase materials have two order parameters: polarization and magnetization. One of the order parameters is generally large and the other is small, which results in minor ME exchange between the two subsystems.

4. Magnetoelectric Composite Materials

Better alternatives to single-phase materials are ME composites that have large magnitudes of ME voltage coefficient. The ME effect can be realized by using composites of piezomagnetic and piezoelectric phases or magnetostrictive and piezoelectric phases. Moreover, these composites are easy to fabricate compared to the single-phase materials, cost-effective, and they have higher working temperature range [2, 25, 26].

5. Properties of Composite

Composite properties can be divided into three categories; sum properties, product properties, and combination properties. A sum property is average of the contribution from individual phases present in the composite such as density, resistivity, and so forth. Product property can be explained as follows: If one phase shows the property $A \rightarrow B$ and the other shows $B \rightarrow C$, then the composite will show new property $A \rightarrow C$. Magnetoelectric effect is product property of the composite. Other examples of product property are piezoresistance (piezoelectric and magnetoresistance), magnetoresistance (magnetostriction and piezoresistance), photostriction (photoconductivity and electrostriction),

and piezoluminescence (piezoelectricity and electroluminescence) [27]. If the average magnitude of the property in composite exceeds the value of the end components, then it is an example of combination properties. If two phases show convex and concave type of sum properties, then the combination of these two will produce a maximum at an intermediate phase composition.

6. Connectivity of Composite

Composite geometry can be designed based upon the connectivity. For two-phase system, there are ten types of connectivity. For three- and four-phase system, there are 20 and 35 types of connectivity. The connectivity in general can be given by the ratio $((n + 3)!/3!n!)$, where n is number of phases. Figure 1 shows the geometry for different connectivities (1-0, 2-0, 3-0, 1-1, 2-1, 3-1, 2-2, 2-3, and 3-3) in two, phase composite. A 3-0 connectivity implies particulate type of composite where one phase will be the matrix and the other phase will be dispersed in the matrix. A 2-2 connectivity represents the layered geometry which can be bilayer, trilayer, or multilayer. The phases are connected in plane but not out of plane. This connectivity is most commonly used for multilayer capacitors and laminated magnetoelectric composite [28].

7. Types of Magnetoelectric Composites

Among various possibilities for magnetoelectric composites, *in-situ*, sintered particulate and nanoparticulate composites are of 0-3 connectivity whereas laminate and multilayer composites are mainly of 2-2 type and the nanopillars are 1-3 composites. In the following subsection, each of the composite systems will be discussed separately with a list of different reported values for ME coefficient.

7.1. In-Situ Composite Using Unidirectional Solidification. The original work on ME composites was done at Philips Laboratories [30–34]. The ME composites were synthesized by unidirectional solidification of eutectic composition in quinary system Fe-Co-Ti-Ba-O. The unidirectional solidification results in decomposition of eutectic liquid into alternate layers of the constituent phases; a piezoelectric perovskite phase (P) and a piezomagnetic spinel phase (S) ($L \rightarrow P + S$). The results showed that presence of excess TiO_2 (1.5 wt%) gives a high ME voltage coefficient of $dE/dH = 50 \text{ mV/cm}\cdot\text{Oe}$ [31]. However, other compositions showed a lower dE/dH in the range of 1–4 $\text{mV/cm}\cdot\text{Oe}$. In subsequent work, a high ME coefficient of 130 $\text{mV/cm}\cdot\text{Oe}$ was obtained for eutectic composition of BaTiO_3 - CoFe_2O_4 by unidirectional solidification [33]. This value is about an order of magnitude higher than that of single phase Cr_2O_3 ($dE/dH = 20 \text{ mV/cm}\cdot\text{Oe}$). However, unidirectional solidification has several complications for implementing in practical applications such as long duration, and it requires critical control over the composition [32]. This type of composite allows forming spinel dendrites in perovskite matrix, which are detrimental for obtaining large piezoelectric and magnetoelectric effect. The resistivity of these *in-situ*

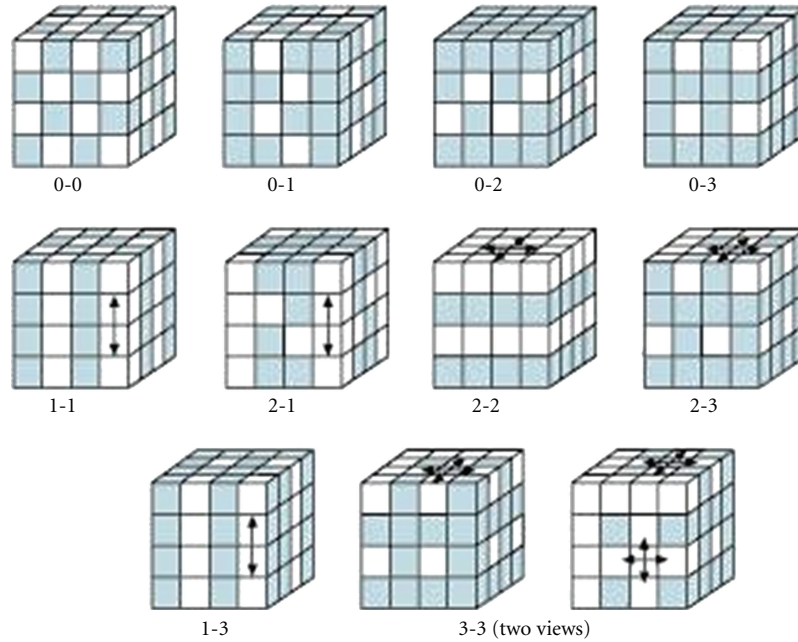


FIGURE 1: Different types of connectivity of the two-phase composite system [28, 29].

composites is very low of the order of 10^8 – $10^9 \Omega\cdot\text{cm}$, which presents difficulty in electrical poling.

7.2. Laminated Composite. Recently, giant ME response has been reported for laminate composites, fabricated by bonding piezoelectric plate/disk/fibers between two layers of magnetostrictive plates/disks/foils [34–37]. Figures 2(a) and 2(b) show the piezoelectric plates or fiber sandwiched between two magnetostrictive plates or foils, respectively. In these designs, the external magnetic field creates strain in the magnetostrictive layers which is transferred on to the piezoelectric material through bonding layer thereby producing electrical charge across the electrodes. The electrical charge is amplified and converted into voltage using a capacitive circuit. A magnetic DC bias of varying magnitude is essential to obtain the magnetostrictive strain. The magnetoelectric laminate composite, embedding piezoelectric PMN-PT single crystal between magnetostrictive Terfenol-D single crystal, exhibited the ME coefficient of $10.30 \text{ V/cm}\cdot\text{Oe}$, which is ~ 80 times higher than that previously reported in either naturally occurring magnetoelectrics or artificially designed composites (ADCs). Srinivasan et al. have investigated the bilayer and multilayer structure of PZT and ferromagnetic ferrites. It was shown that multilayer structures can provide ME coefficient as high as $1500 \text{ mV/cm}\cdot\text{Oe}$ [38, 39]. Laminated structures of Ni-PZT-Ni were found to exhibit ME coefficient of 400 – $450 \text{ mV/cm}\cdot\text{Oe}$ [40]. Three-phase composites of PZT/epoxy/Terfenol-D or PZT/PVDF/Terfenol-D have been reported to possess the ME coefficient in the range of 50 – $150 \text{ mV/cm}\cdot\text{Oe}$ [41]. Dong et al. have reported composite structures consisting of piezofiber laminated between two three-phase composites of PZT/epoxy/Terfenol-D or PZT/PVDF/Terfenol-D have been reported and the magnitude of ME coefficient was found to be in the range of 50 – 150

$\text{mV/cm}\cdot\text{Oe}$ [41]. Dong et al. have reported composite structure consisting of piezofiber laminated between two sheets of high-permeability magnetostrictive FeBSiC alloys [42]. This structure exhibited a giant response of $22 \text{ V/cm}\cdot\text{Oe}$ at 1 Hz.

7.3. ME Micro/Nanostructures. Recently, magnetoelectric composite-based nanostructures have been synthesized using thin-film deposition techniques such as sol-gel deposition, PLD, and RF magnetron sputtering. The commonly experimented geometries are bilayers, heterostructures, self-assembled structures, and nanowires. Zheng et al. have synthesized the self-assembled nanostructure in BaTiO_3 - CoFe_2O_4 [BTO-CFO] composite system consisting of CFO nanopillars embedded in BTO matrix [8]. TEM investigation of self-assembled nanopillars show 20 – 30 nm CFO pillars embedded in BTO matrix. Compared to bulk ME composites, nanostructures offer the possibility of much higher interlayer interaction. The disadvantage of nanopillars is high leakage current due to continuous path of low-resistance ferrite pillars. The multilayer geometry has a disadvantage of clamping effect of the substrate. ME nanoscale heterostructures of PZT-CFO double-layer thin films, PZT-NFO nanoparticulate composites, and PZT-CFO nanowires have also been reported [44]. Figure 3 shows the HRTEM and cross-sectional TEM of 4 different systems. Figure 3(a) shows the HRTEM image of BTO-NFO heterostructure with sharp SAED pattern in the inset. The misfit strain is around -0.8% which is smaller than that for bulk ceramics. The lattice constant calculated from SAED pattern was 3.943 and 4.023 \AA for BTO and 8.244 \AA for NFO [45]. Figure 3(b) shows the cross-sectional HRTEM for PZT-CZFO composite thin film. Clear interface between PZT and CZFO was observed as well as the interface between the CZFO and

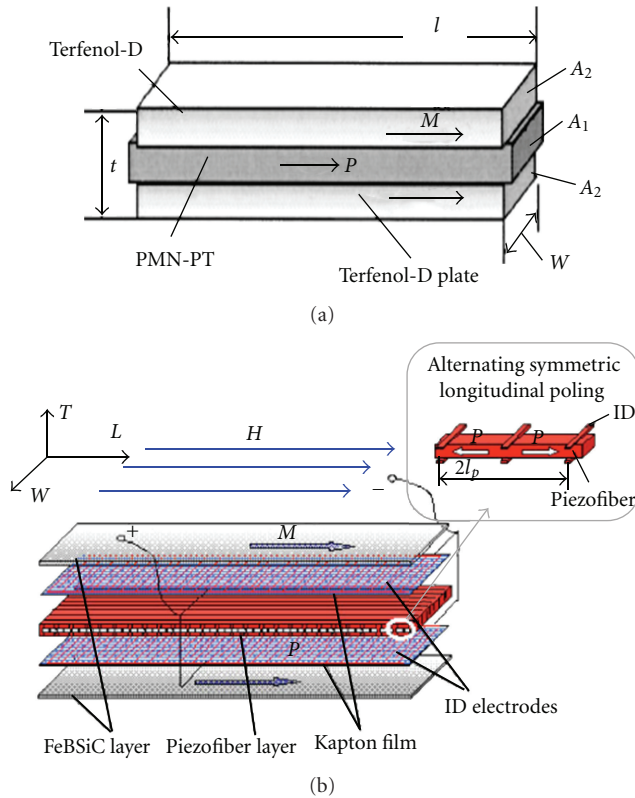


FIGURE 2: Schematic diagram of laminated composite (a) Terfenol-D sandwich structure with PMN-PT in the middle and (b) Magnetic FeBSiC top and Bottom layer with intermediate layer as piezoelectric fiber [42, 43].

the substrate. No evidence of second phase was found in these layered films by HRTEM. In the same literature, it was found that if the PZT was deposited earlier, then it has a preferential growth along the (100) crystallographic orientation [46]. Figure 3(c) shows the HRTEM image of PZT-NFO nanoparticulate composite thin film. Clearly a well-defined boundary with different atomic arrangements was observed in this kind of composite which indicates good dispersion of NFO particles in PZT matrix [47]. The cross-sectional TEM image shown in Figure 3(d) corresponds to PZT (440 nm) LSMO (330 nm) bilayer deposited on top of (001) LaAlO₃ substrate. There were large amounts of void grain boundaries observed in LSMO phase, which may help to release the magnetostrictive strain along the normal of the plain direction [48].

7.4. Sintered Composites. Magnetolectric (ME) effect in particulate sintered composites has generally been obtained by combining magnetostrictive and piezoelectric phases. Sintered composites fabricated by mixing of piezoelectric and ferromagnetic phases have been widely studied because of its simplicity in synthesis using well-established conventional ceramic processing technique. Various particulate composites of piezoelectric (BaTiO₃ or Pb(Zr,Ti)O₃) and magnetostrictive (LiFe₅O₈, Ni_{1-x}Zn_xFe₂O₄, CoFe₂O₄, or CuFe₂O₄) phases with different dimensional connectivity's

have been reported in literature. Although the ME effect is known in various binary systems, little information is available on structure-property relationship. Sintered particulate composites have inferior properties compared to laminated ones because of drawbacks of low resistivity, interface defects, interface diffusion, and mismatch of elastic compliances. To enhance the ME coefficient of sintered composite, it is necessary to optimize the composition, microstructural features (grain size, grain orientation), and sintering parameters. In particulate composites, higher ME coefficient implies higher elastic coupling between the magnetic and piezoelectric phases. The elastic coupling can be maximized by having coherent response from the magnetostrictive phase under dc bias, so that the stress on the piezoelectric lattice across the grains is in phase with each other. This is only possible if there is uniform distribution of the magnetostrictive phase with soft piezoelectric phase. If the particles are crystallographically aligned with the matrix, more benefits can be obtained because of the built-in directionality. However, this is quite difficult to obtain in practice. An attempt has been made to achieve this by synthesizing textured composites. In addition to conventional ceramic processing and sol-gel route, one pot [49] is a process where the two phases are simultaneously synthesized in the same pot in order to get better homogenization and dispersion of magnetic phase. Heterocoagulation has been demonstrated to provide the core-shell structures of ferroelectric and ferromagnetic composite particles. Heterocoagulation process consists of coagulation of particles with opposite surface charges dispersed in a solution. At some specific pH value, one species has a positive surface charge density whereas the other one has a negative charge.

8. Problems and Shortcoming of Sintered Composite

The trend of the ME research since 2002 is to use a high magnetostriction material (Terfenol-D) or a high permeability material (Metglas) and use epoxy to bond with a PZT plate, rod, disk, fiber, and so forth. Different piezoelectric vibration modes such as bending, longitudinal, radial, and push-pull and so forth. have been utilized in laminated geometries. However, these reported structures have so far failed to identify the synthesis process that can eliminate the need for epoxy. Practically, industry would like to have a ceramic composition with relatively simple processing technique that can provide higher sensitivity. In order to get higher ME coefficient, the following problems needs to be addressed.

- (1) How can the ME coefficient be enhanced in the bulk sintered composites?
- (2) What are the microstructural variables that make significant contribution towards ME coefficient?
- (3) Define a composition space that allows identification of specific elements providing enhanced ME coefficient.
- (4) Define the geometry of the sintered composite that will lead to better coupling in dual phase structures.

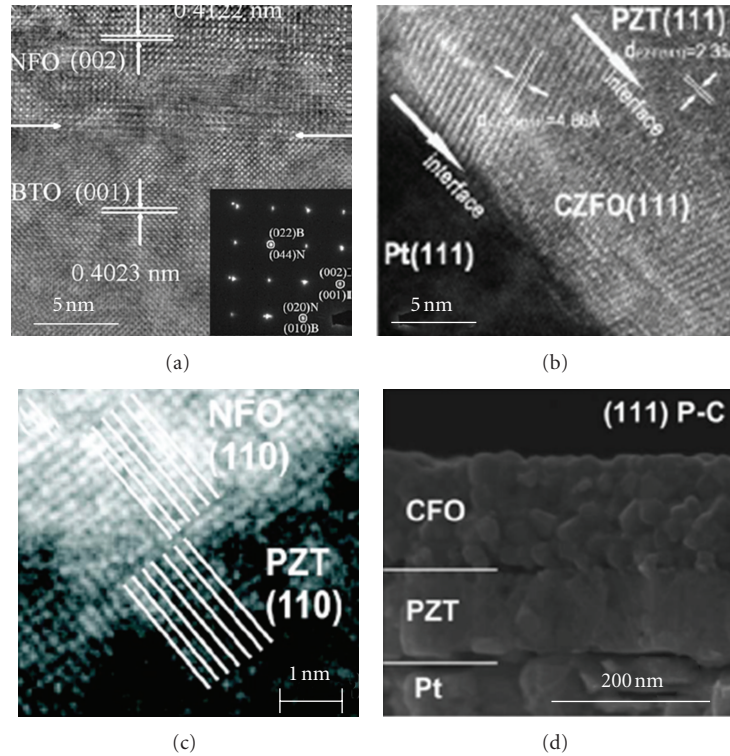


FIGURE 3: (a) HRTEM of BTO-NFO bilayer thin-film structure, (b) HRTEM of PZT-CZFO bilayer thin-film structure showing interface, (c) HRTEM of PZT-NFO nanoparticulate composite showing orientation relationship of NFO (110), and PZT (110), and (d) cross-sectional TEM image of PZT-CFO bilayer film [45–48].

- (5) Establish the composition-microstructure-property relationships for dual phase sintered composites.

In order to solve these problems, several factors need to be investigated [1–31].

- (1) Effect of the piezoelectric and magnetostrictive composition.
- (2) New microstructures that can provide enhanced resistivity.
- (3) Processing steps that can provide equilibrium between the two phases.
- (4) Removal of defects at the piezoelectric—magnetostrictive interface formed due to mismatch in shrinkage rate and sintering temperatures of individual phases.
- (5) Control of grain size and orientation.
- (6) Periodic distribution of two phases.
- (7) Geometry of the phase distribution.

A significant effort is required to address the above-mentioned factors. Realization of sintered composite with large ME coefficient will provide an adequate energy conversion device from magnetic to electric. In addition to magnetic field sensing and current probes, various other commercial applications are possible such as gyrotator, read-only memory device, transducers, filters, recording heads,

and sensors. Magnetoelasticity in two-phase (piezoelectric-magnetostrictive) composite is a strain mediated effect where magnetostrictive strain produced by applied magnetic field is transferred on to the piezoelectric phase. In order to achieve efficient strain transfer, piezoelectric materials with matching elastic properties and higher piezoelectric voltage constant (g) are suitable. The mechanical properties of PZT-based ceramics are nearly similar for various compositional modifications. However, the electrical properties can be changed to a large extent by tailoring the microstructure, defect concentration, and domain states. Figure 4 shows the design concept for a high-performance magnetoelastic composite. The prime requirement for this composite is high piezoelectric voltage constant, low loss material. This goal correlates with the design of high-energy density material as it will be shown here that the coefficients for energy are dependent on “ g ” constant.

9. Scope of this Review

The scope of improvement is in meeting with the challenges of sintering which lead to low ME coefficient as identified in previous sections. First of all, chemical reaction, low resistivity, and interface defects such as porosity, micro cracks make very weak coupling between the piezoelectric and magnetostrictive phase. Secondly, if the resistivity of the composite is low, electrical poling becomes very difficult due to high leakage current. Lastly, the connectivity of

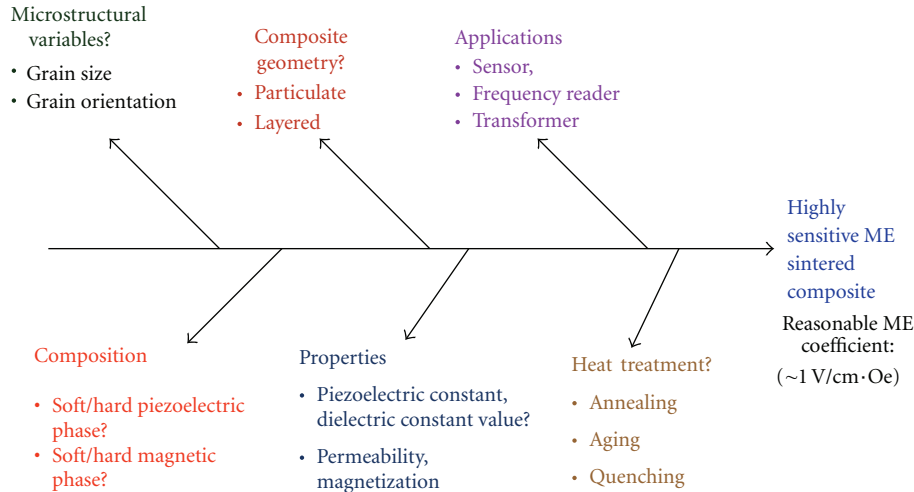


FIGURE 4: Fish-bone diagram for solving ME sintered composite issues.

the ferrite grains plays an important role. Good dispersion of ferrite grains inside the piezoelectric matrix is essential for sustaining sufficient electrical resistivity in the matrix. To further improve the property of the composite, comprehensive understanding of each parameter that controls the magnetoelectric coefficient is necessary and efforts have to be made to optimizing these controlling variables. Also the fabrication process for the composites should be designed to provide a cost-effective ME composites. ME composites can lead to miniaturization of several electronic components and thus cost-effective methodology will facilitate their deployment. Magnetolectric MEMS devices can be designed to enhance the functionality of the system.

To understand the science of magnetolectric materials and hence to synthesize the composite with high ME response an optimum system with best possible composite geometry needs to be realized. To start with, the selection of appropriate composition with suitable doping is the important step. The effect of microstructural features, sintering parameters, and heat treatment on the ME response should be analyzed. The specific factors that need to be considered are as following.

9.1. System Selection. The figure of merit for large magneto-electric coefficient in a ferromagnetic-ferroelectric composite is given by the (14) as

$$\text{Figure of merit} = \sqrt{\mu\epsilon}, \quad (14)$$

where μ is the magnetic permeability and ϵ is the dielectric permittivity. Thus, the primary criterion for the selection of the individual phases in the composite is to identify materials having similar crystallographic symmetry and possessing large magnetic permeability and dielectric permittivity. As is well known that compared to BaTiO_3 (BT), $\text{Pb}(\text{Zr Ti})\text{O}_3$ [PZT] has stronger piezoelectric and dielectric properties, higher Curie temperature, higher resistivity, and lower sintering temperature. Also there is no high-temperature phase transition in the PZT system. Investigations have shown that

the nickel-based ferrite particles are very stable in the doped-PZT matrix and do not react at high sintering temperatures of 1250°C [50]. Ni-based ferrites are soft compared to Co-ferrite and have higher permeability. Also an addition of Zn in the ferrite structure improves the permeability, magnetization and reduces the Curie temperature. Thus, PZT and Ni ferrite satisfies the phase equilibrium criterion for large ME effect.

9.2. Composition of Multiphase System. Composition of the piezoelectric and magnetostrictive phase needs to be optimized. For piezoelectric phase using PZT as the base composition, the composition can be varied using acceptor or donor dopant. Acceptor dopants (Mn, Zn, etc.) result in decreased piezoelectric, dielectric constant, and dielectric loss. On the other hand, donor dopants (Nb) are higher in valance and create cation vacancies, resulting in increased piezoelectric and dielectric constant with increased loss. The composition for ferromagnetic phase can be varied to change the magnetic properties such as magnetization, permeability, and coercivity. Ni- and Co-based ferrites are the base composition because ferrites have higher resistivity than metallic ferromagnets. To improve the resistivity, Mn can be doped, and to increase the magnetization, Zn can be doped.

9.3. Microstructural Features: Grain Size. Effect of grain size on piezoelectric, dielectric, and ferroelectric properties has been widely studied in literature [51–55]. It is well known that piezoelectric and dielectric properties drop rapidly below critical grain size (~ 100 nm) [56, 57]. SEM analysis combined with the surface tension measurement indicate that the surface bond contraction due to small size induces a compressive stress on the inner part of a grain and this effect plays an important role in ferroelectric materials in the nanometer size range. The induced stress causes decrease of Curie temperature and spontaneous polarization with decreasing grain size. The domain wall contribution

has an opposite effect as compared with the surface bond contraction-induced effect. When the grain size decreases to a value comparable to the width of domain walls, pinning points develop inside the grains and the domain wall motion is inhibited. The reduced wall mobility causes a decrease in the relative permittivity. The measured value is a competition between the increase of relative permittivity by the surface bond contraction effect and its decrease by the domain wall pinning effect.

Although the effect of grain size on piezoelectric, dielectric, and ferroelectric properties has been studied, the effect of microstructure on magnetoelectric property has not been studied in detail. As it is well known that the magnetoelectric property depends upon the piezoelectric and dielectric property, which in turn depends on grain size, magnetoelectric property should also depend upon grain size. Optimization of the grainsize will lead to the increased ME coefficient of the composite.

9.4. Microstructural Features: Texturing. Crystallographic texturing of piezoelectric grains in certain orientation can improve the piezoelectric, ferroelectric response because better spontaneous polarization can be achieved than in randomly oriented grain. Many researchers have reported the improvement of piezoelectric responses by incorporating the textured grain growth in the ceramic structure [58–60]. The most common fabrication processes for texturing are hot forging, hot pressing, gradient sintering, and templated grain growth. Templated grain growth is the most popular grain orientation technique, where a seed crystal is added to the matrix containing much finer equiaxed powder. During sintering, the matrix densifies around the templates with the same orientation as that of the templates.

9.5. Composite Geometry. In bulk composite, the resistivity of the composite drops rapidly as the connectivity of the ferrite particles forms a conductive path along the sample. This allows charge leakage through the ferrite. Also, the flux lines cancel each other resulting in a low stress generation. Layered structures are much more attractive as the stress generation is much higher and each phase preserves its physical properties. Also in applications like magnetic field sensing devices, two factors should be clearly addressed: (i) variation of the magnetoelectric (ME) response as a function of the magnetic field direction, and (ii) variation of the ME response as a function of the DC bias. Ideally, the ME response should be a high number without any DC bias. In order to fabricate miniaturized sensors, the approach based on cofiring is more attractive similar to that of multilayer ceramic capacitors.

9.6. Postsinter Heat Treatment. For high magnetoelectric coefficient, homogenized piezoelectric grain, even-distribution of magnetostrictive particle, stress-free interface, and most importantly an equilibrium structure are necessary. A postsintering treatment is necessary to promote the equilibrium condition and to reduce the stress arising from the misfit strain [61–63]. Optimized annealing and

aging condition improve the individual piezoelectric and ferromagnetic properties.

10. Specific Results

As mentioned earlier, it is important to understand the factors controlling the magnetoelectric coefficient. Experimental investigation was conducted to identify the correlation between composition, microstructure, and property. The optimization was conducted in terms of magnetoelectric coefficient (mV/cm·Oe) with supporting structural, electrical, and magnetic characterization.

11. High-Energy Density Piezoelectric Phase for ME Composites

The magnitude of the transduction is governed by the effective piezoelectric strain constant, d , and the effective piezoelectric voltage constant, g . Using the linear constitutive piezoelectric equations, a relation between the energy density of the piezoelectric material and the transduction coefficient (d, g) under an applied stress X can be derived. Under an applied force ($F = X \cdot A$, where A is the area), the open circuit output voltage (V) of the ceramic is given as

$$V = E \cdot t = -g \cdot X \cdot t = -\frac{g \cdot F \cdot t}{A}, \quad (15)$$

where t is the thickness of the ceramic, E is the electric field, and g is the piezoelectric voltage coefficient given as

$$g = \frac{d}{\epsilon_0 \epsilon^X}, \quad (16)$$

where ϵ^X is the dielectric constant under constant stress condition. The charge (Q) generated on the piezoelectric ceramic is given by the relation:

$$D = \frac{Q}{A} = \frac{E}{\beta^X} = \frac{V \cdot \epsilon_0 \epsilon^X}{t}, \quad (17)$$

or

$$\frac{Q}{V} = \frac{\epsilon^X \epsilon_0 A}{t} = C, \quad (18)$$

where D is the dielectric displacement, C is the capacitance, and ${}^X\beta$ is the dielectric susceptibility of the material under constant stress condition. Dielectric susceptibility is equal to the inverse of dielectric permittivity tensor component and can be defined from the constitutive equation for a linear piezoelectric material as

$$E = -g X + \beta X D. \quad (19)$$

Equation (18) shows that at low frequencies, a piezoelectric plate can be assumed to behave like a parallel plate capacitor. Hence, electric energy available under ac stress excitation is given as $U = 1/2CV^2$ or energy per unit volume

$$u = \frac{1}{2} (d, g) \cdot \left(\frac{F}{A}\right)^2. \quad (20)$$

Equations (15) and (20) show that for a given material of fixed area and thickness, a material with high (d.g) product and high g constant will generate high voltage and power when the piezoelectric ceramic is directly employed for mechanical to electrical energy conversion. Since, in the case of magnetoelectric composites, the magnetostrictive phase applies the stress on the piezoelectric phase through elastic coupling the high-energy density material will lead to higher response.

12. Design of High “g” Materials

Enhancement in the magnitude of the piezoelectric voltage constant requires an optimization in the magnitude of the piezoelectric stress constant and dielectric constant. In general, the variation in the magnitude of piezoelectric stress constant and dielectric constant is similar and they increase or decrease simultaneously upon modification with dopants or processing technique resulting in minor changes in the magnitude of their ratio. A novel processing strategy is required to obtain large g constants [64]. The criterion for maximization of the product (d.g) with respect to the microstructure variable x (such as grain size) can be determined as follows:

$$\begin{aligned} \frac{\partial}{\partial x}(\text{d.g}) &= d \cdot \left(\frac{\partial g}{\partial x} \right) + g \cdot \left(\frac{\partial d}{\partial x} \right) \\ &= 2 \cdot \left(\frac{d}{\varepsilon} \right) \cdot \left(\frac{\partial d}{\partial x} \right) - \left(\frac{d}{\varepsilon} \right)^2 \left(\frac{\partial \varepsilon}{\partial x} \right) = 0 \end{aligned} \quad (21)$$

or

$$\frac{\partial(\ln d^2)}{\partial x} = \frac{\partial(\ln \varepsilon)}{\partial x} \implies d = \varepsilon^{0.5}, \text{ where } \varepsilon = \varepsilon^X \varepsilon_0. \quad (22)$$

Once again, differentiating (21) with respect to x and substituting the condition given by (22), it can be shown that

$$\left(\frac{\partial^2}{\partial x^2} \right) (\text{d.g}) = \left(\frac{\partial \varepsilon}{\partial x} \right)^2 \frac{1}{\varepsilon^{1.5}} \left(1 - \frac{1}{\varepsilon^{0.5}} \right) < 0. \quad (23)$$

Thus, the condition given by (22) represents the maximum magnitude of the product (d.g). In general, the condition given by (22) can be expressed as [64]

$$|d| = \varepsilon^n. \quad (24)$$

Using (24), the maximum magnitude of the product (d.g) is given as

$$\text{Max}(\text{d.g}) = \varepsilon^{2n-1}, \quad (25)$$

where n is the material constant which is fixed by the magnitude of the piezoelectric and dielectric constants. It has been shown that for all the commercial polycrystalline ceramic materials, the magnitude of n lies in the range of 1.1 to 1.3, (24) represents a deterministic rule for realizing the high-energy density piezoelectric materials. According to this equation, a giant enhancement in the magnitude of the g constant will be obtained by reducing the magnitude of the n . As the magnitude of n decreases and approaches the

theoretically minimum possible value of 0.5, the magnitude of product (d.g) reaches the maximum possible magnitude of unity. In order to obtain large magnitude of the product (d.g), the piezoelectric compositions can be tailored by modifying with the dopant or processing technique such that the change in piezoelectric and dielectric constant leads to a decrement in the magnitude of constant n .

The piezoelectric constant, d , can be written in terms of the electromechanical coupling factor, k , and the elastic compliance, s , as follows:

$$d = k \sqrt{\varepsilon \cdot s}. \quad (26)$$

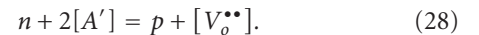
Substituting (24) into (26), it can be shown that

$$n - \frac{1}{2} = \frac{\ln(k)}{\ln(\varepsilon)} + \frac{1}{2} \frac{\ln(s)}{\ln(\varepsilon)}. \quad (27)$$

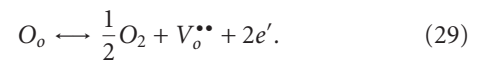
Equation (27) indicates that a material with low magnitude of n will require low magnitude of coupling coefficient and elastic compliance. However, large coupling factor and low losses are important for efficient energy conversion.

13. Defect Chemistry

Defects and substituents are known to affect the electromechanical properties of the normal ferroelectrics in both poled and unpoled conditions [65–70]. Generally, acceptor doping (Fe, Mn, Ni, Co) in the PZT-based ceramics results in (i) decreased dielectric constant and loss, (ii) lower elastic compliance, (iii) lower electromechanical coupling factor, and (iv) lower electromechanical losses. In contrast, donor doping (La, Sb, Bi, W) results in (i) increased dielectric constant and loss, (ii) increased elastic compliance, (iii) increased electromechanical coupling factor, and (iv) increased electromechanical losses. Thus, an acceptor modified material seems to be appropriate for obtaining low value of n . In acceptor modified materials, oxygen vacancies are created for charge compensation, which are frozen into the ceramic during quenching from high temperature. The electroneutrality reaction representing the equilibrium between acceptor ions (A) and oxygen vacancies is expressed as



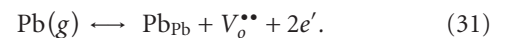
Assuming a constant lead activity, the formation of oxygen vacancy can be expressed as



The rate constant for this reaction can be expressed as

$$K = [V_o^{\bullet\bullet}] \text{PO}_2^{1/2} e^2, \quad (30)$$

where PO_2 is the partial pressure of the oxygen. If PO_2 is constant, then the formation of $V_o^{\bullet\bullet}$ can be expressed as:



These oxygen vacancies can reside in the material in many possible ways: (i) associated defect dipole structure with acceptor, (ii) diffuse to domain walls, or (iii) compensate the local charge fluctuation at domain walls. The mechanism for introduction of “hard” properties depends on the way in which oxygen vacancies distribute themselves. In Mn-modified PZT ceramics, it is believed that hardening occurs due to the pinning of domain boundaries by Mn—oxygen vacancy defect structure [67]. Further, it is believed that Mn^{+3} attaches strongly to oxygen vacancies due to Jahn Teller effect. This prevents conduction and reduces the domain wall mobility resulting in reduced losses [65]. The MPB ($\text{Zr}:\text{Ti} = 52:48$) composition in PZT shows the highest piezoelectric properties such as high piezoelectric constant d_{33} , coupling factor k , and dielectric constant. These properties drop on either side of the MPB. The compositions on tetragonal side ($\text{Zr}:\text{Ti}$ ratio of 56:44) have less variation in the dielectric and piezoelectric properties as compared to composition on the rhombohedral side with reference to MPB [71]. Thus, by selecting a composition on the tetragonal side and doping with suitable donor (Nb^{+5} , etc.) and acceptor (Zn^{+2} , Ni^{+2} , etc.) ions, it is possible to formulate a composition, which has relatively higher piezoelectric constant d_{33} but lower dielectric constant.

14. Effect of Doping: Piezoelectric Phase

Different piezoelectric composition can be fabricated using hard and soft characteristics. Two different compositions such as $0.9 \text{ Pb}(\text{Zr}_{0.52}\text{Ti}_{0.48})\text{O}_3 - 0.1 \text{ Pb}(\text{Zn}_{1/3}\text{Nb}_{2/3})\text{O}_3$ [PZT(soft)] and $0.9 \text{ Pb}(\text{Zr}_{0.56}\text{Ti}_{0.44})\text{O}_3 - 0.1 \text{ Pb}[(\text{Zn}_{0.8/3}\text{Ni}_{0.2/3})\text{Nb}_{2/3}]\text{O}_3 + 2 \text{ (mol \%)} \text{ MnO}_2$ [PZT (hard)] were used to see the effect of soft and hard nature of PZT on magnetoelectric coefficient. The magnetostrictive phase was fixed at 20 mole% $\text{Ni}_{0.8}\text{Zn}_{0.2}\text{Fe}_2\text{O}_4$. It was found that as the composition becomes electrically and mechanically soft, the polarization increases. Figure 5(a) shows that the polarizations of PZT, PZT (hard), and PZT (soft) were recorded as 14.61, 23.54, and $31.65 \mu\text{C}/\text{cm}^2$, respectively. As we dope the PZT with Nb, the structure becomes softer, and therefore, piezoelectric, dielectric property increases. This also affects the piezoelectric, dielectric, and magnetoelectric properties of the composite. Piezoelectric constant (d_{33}) increases from 72 to $125 \text{ pC}/\text{N}$ and dielectric constant increases from 635 to 915. From Figure 5(b), it is clearly observed that the PZT (soft)-20 NZF shows the maximum magnetoelectric response of $186.49 \text{ mV}/\text{cm}\cdot\text{Oe}$, whereas pure PZT shows the value of $127.96 \text{ mV}/\text{cm}\cdot\text{Oe}$, an increase of about $\sim 50\%$. Corresponding elastic compliances (S_{11}) of these two compositions are 1.11×10^{-11} and $1.734 \times 10^{-11} \text{ m}^2/\text{N}$ —this data indicates a simple metric that softer the materials better is the magnetoelectric response.

15. Effect of Doping: Magnetostrictive Phase

Magnetic property, such as saturation magnetization and coercivity, controls the magnetoelectric property of the composite. A soft high initial permeability magnetic phase

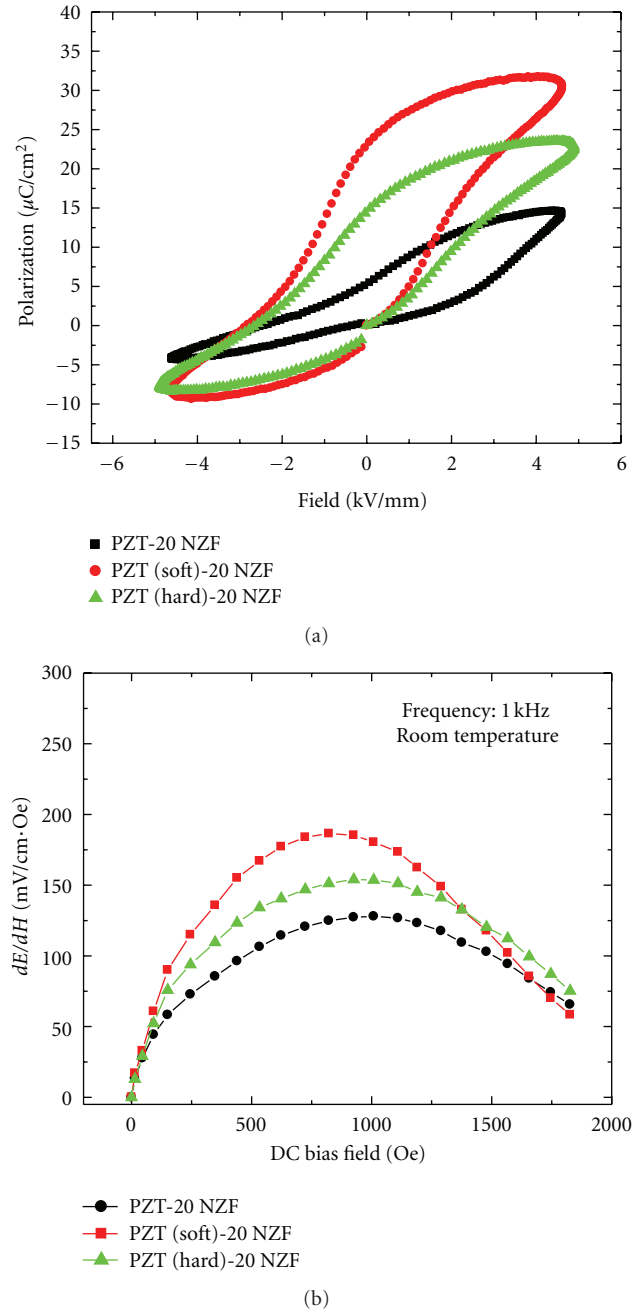
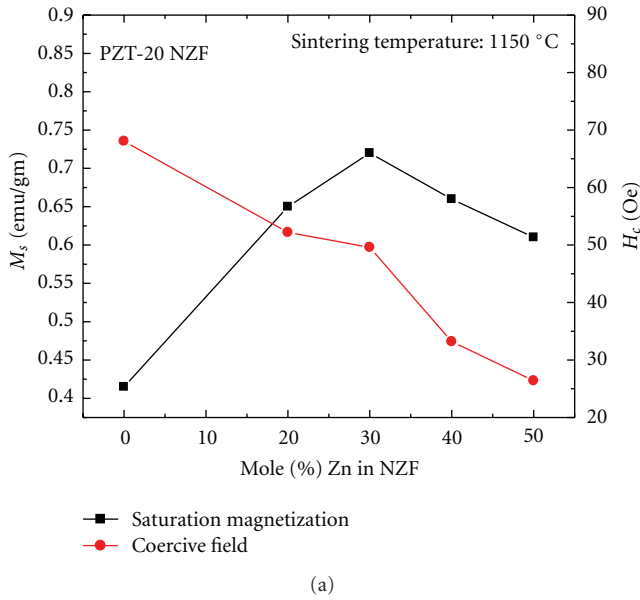
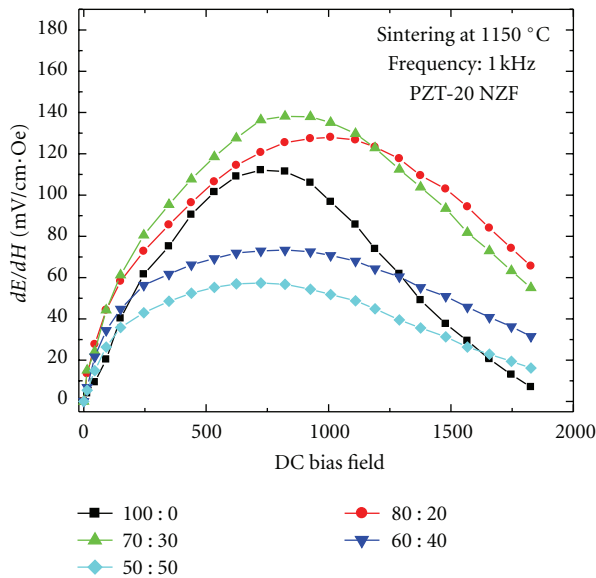


FIGURE 5: Effect of piezoelectric phase on the saturation polarization and magnetoelectric coefficient of ME composites.

with magnetostriction will lead to larger domain rotation. Saturation magnetization is directly related to the permeability and the magnetostriction. The higher the magnetization, the higher is the permeability and the magnetostriction. Several compositions such as $\text{NiFe}_{1.9}\text{Mn}_{0.1}\text{O}_4$ (NFM), $\text{Ni}_{0.8}\text{Zn}_{0.2}\text{Fe}_2\text{O}_4$ (NZF), CoFe_2O_4 (CFO), and $\text{Co}_{0.6}\text{Zn}_{0.4}\text{Fe}_2\text{O}_4$ (CZF) have been studied and it was found that the $\text{Ni}_{0.8}\text{Zn}_{0.2}\text{Fe}_2\text{O}_4$ has the smallest coercivity (52 Oe) and also it has the largest magnetoelectric coefficient. CFO is magnetically hard (coercivity 318.34 Oe) compared



(a)



(b)

FIGURE 6: Effect of Zn doping on magnetic and magnetoelectric properties of PZT-20 NZF.

to NZF and has very small magnetolectric response due to limits in domain wall rotation. Also, the control of Zn doping has a major effect of the magnetic property. It was found from Figure 6(a) that with the increase in Zn concentration, the coercivity drops. But the magnetization shows maxima at 30% Zn doping. The optimum concentration of Zn doping was found to be 30 mole%, at which the highest saturation magnetization was observed with moderate coercivity. At this composition, high ME coefficient of 144 mV/cm·Oe was recorded as observed from Figure 6(b)—an increase of about 25%.

16. Effect of Grain Size

Figures 7(a)–7(d) show the SEM microstructure of ME composite with 830, 758, 111, and 97 nm average grain size, respectively. All the microstructures were found to be dense and well sintered. The density data shows that as the grain size of the composite decreases the density increases, and at grain size of 97 nm the densification reaches about 98%. The densification decreases to 93% as the grain size increases to 750 nm. Figure 8(a) shows the variation of longitudinal piezoelectric strain constant (d_{33}) and dielectric constant (ϵ_r/ϵ_0) with grain size. It can be noticed in this figure that there is a critical grain size below which the piezoelectric properties drop rapidly. The critical grain size is in the range of 100–150 nm. Above 200 nm, the piezoelectric properties increase slowly and saturate at 600 nm. The magnitude of d_{33} and ϵ_r/ϵ_0 for ME composite with grain size of 97 nm were 44 pC/N and 659. This magnitude increases rapidly to 65 pC/N, and 746 at grain size of 215 nm. Above 600 nm, the piezoelectric and dielectric properties saturate at the magnitude of 72 pC/N and 781. The increase in the piezoelectric and dielectric properties can be explained in terms of domain wall motion. For larger grains, where the size of the domain is smaller than the size of the grains, the movement of the domain walls is easier. On the other hand, in small grains, the movement of domain walls is restricted by the grain boundary. As a result during poling, the domain switching will be difficult which reduces the piezoelectric properties [52–72]. Figure 8(b) shows the variation of the ME coefficient as a function of the grain size. As the grain size decreases, ME coefficient drops and shows similar trend as that of piezoelectric property. Above 200 nm grain size, the ME coefficient increases and it saturates above 600 nm as shown in Figure 8(b). For the grain size of 97 and 830 nm, the ME coefficient was found to be as 54.4 and 157.5 mV/cm·Oe, respectively. So, it can be noticed that larger grain size of around 1 μ m or more will enhance the magnetolectric property.

17. Effect of Geometry

In particulate composite, as the piezoelectric and magnetostrictive particles are randomly mixed, a large number of interfaces are created. It was found in our previous studies that at the interfaces of eutectic-based BaTiO₃-CoFe₂O₄ (BTO-CFO) composite, elemental interdiffusion occurs. In the BTO-30 CFO composite, where BTO rich islands were observed in BTO-CFO matrix, considerable amount of interdiffusion occurs. Elemental mapping of Co and Fe show that Fe and Co have diffused through BaTiO₃. Therefore, it is advantageous to create artificial interfaces as bilayer, trilayer, and so forth. The advantages of these types of artificial interfaces are interdiffusion is reduced; resistivity is high, less chance of chemical reaction, and piezoelectric/magnetostrictive properties are higher. Figure 9(a) shows the high magnification interface microstructure of PZT (hard)-Ni_{0.6}Zn_{0.2}Cu_{0.2}Fe₂O₄ (NCZF) cofired bilayer composite observed using Zeiss Leo Smart SEM on the polished and thermally etched samples. The

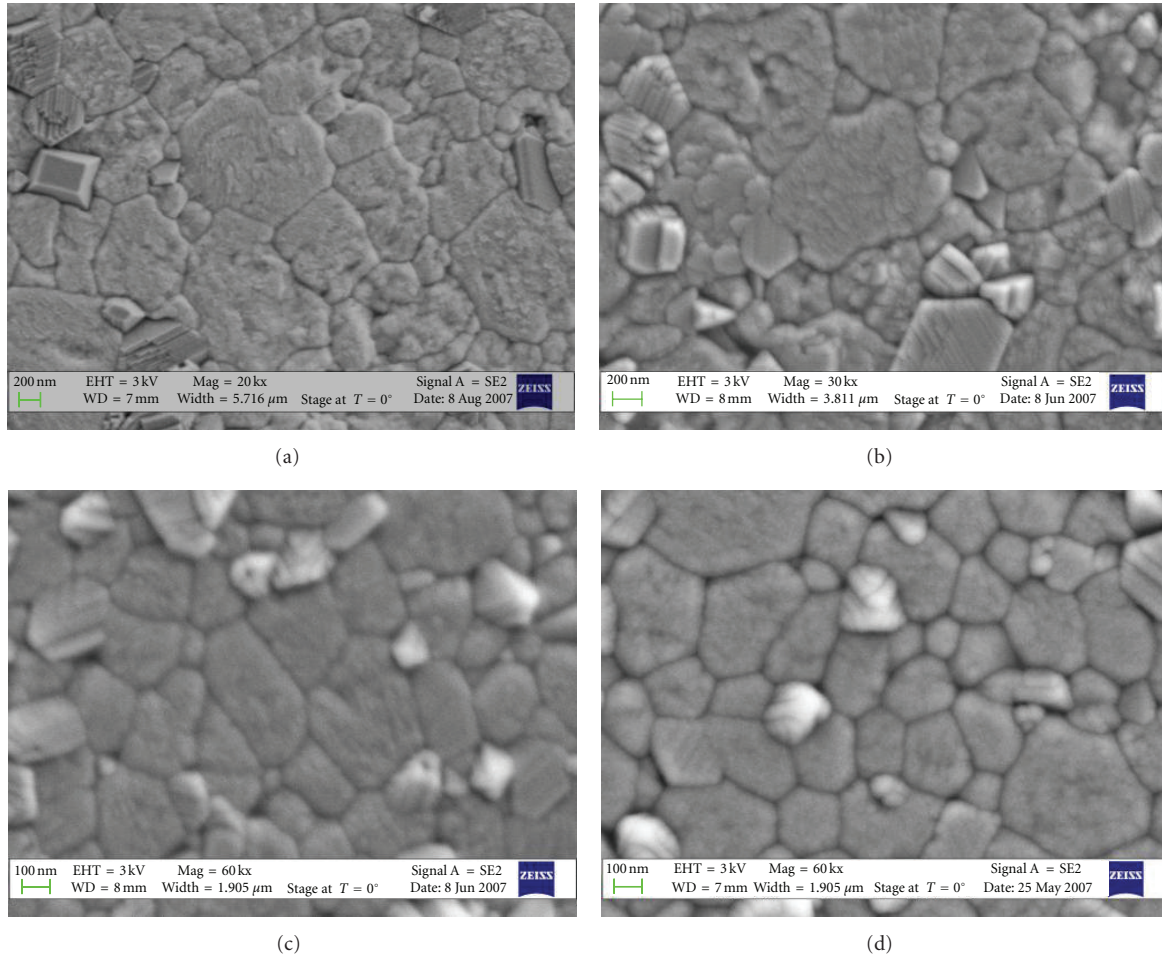


FIGURE 7: Microstructures of ME composites with varying grain size (a) 830 nm, (b) 758 nm, (c) 111 nm, and (d) 97 nm.

PZT grain size in the vicinity of the interface was larger than the grains far away from the interface. Liquid-phase sintering was found to occur in the PZT phase near the interface which may be associated to the diffusion of Cu at the interface and formation of low melting temperature phase. A low magnification microstructure of the interface showed the presence of porosity along the interface. An SEM elemental mapping of Cu shows that more concentration of Cu was found in the PZT phase close to interface which may be responsible for the liquid phase sintering [73–75]. Figure 9(b) shows the ferroelectric property of the cofired bilayer composite. Polarization of $60 \mu\text{C}/\text{cm}^2$ and 0.1% strain was recorded at 4.5 kV/mm.

A square P-E loop was measured for the bilayer which signifies the high resistivity. The shape of the strain versus electric field loop was a normal butterfly loop observed for PZT. Figure 10(a) compares the magnetization-magnetic field hysteresis curve of bilayer and bulk composites measured with an alternating gradient magnetometer (AGM) up to 1.4T. It was found that the saturation magnetization (M_s) is higher in bilayer composite than the bulk, and the coercivity (H_c) drops from 43 Oe to a very low magnitude of 2.8 Oe. Figure 10(b) shows the temperature dependence

of magnetization for bilayer and bulk composites measured in a high-temperature oven installed with Quantum design physical property measurement system (PPMS). The magnetic Curie temperature (T_c) was determined from the intersection of extrapolations of the greatest slope and flat region above T_c . It was found that T_c of the bilayer composite was higher than that of bulk composite. It can be noticed from Figure 10(b) that the magnetization-temperature behavior of the bilayers shows a change in slope at 530 K ($\sim 257^\circ\text{C}$). This temperature range is similar to where peak in the dielectric behavior was observed. The results indicate the presence of secondary phase in the bilayer composites which is reflected both in dielectric and magnetic properties. This transition could be related to the presence of $\text{Cu}_2\text{O}/\text{CuO}$ or a second ferromagnetic phase evolving from CuFe_2O_4 which forms a gradient composite structure with the PZT. Shrotri et al. have shown that doping above 20 mole % Cu in $(\text{Ni},\text{Zn})\text{Fe}_2\text{O}_4$ makes it unstable and at first CuO starts to form followed by a secondary-phase corresponding to the formulation CuFe_2O_4 [76, 77]. The free CuO if present on the piezoelectric side will react with the PZT-PZN to form low-temperature melting composition which is commonly observed in the low-temperature sintering of

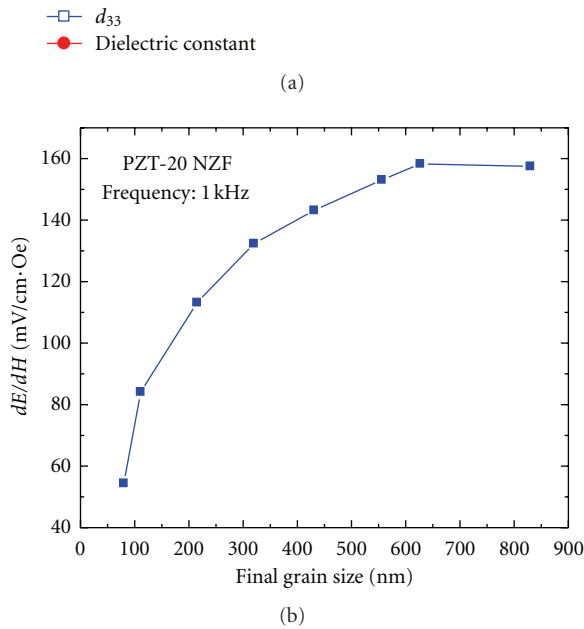
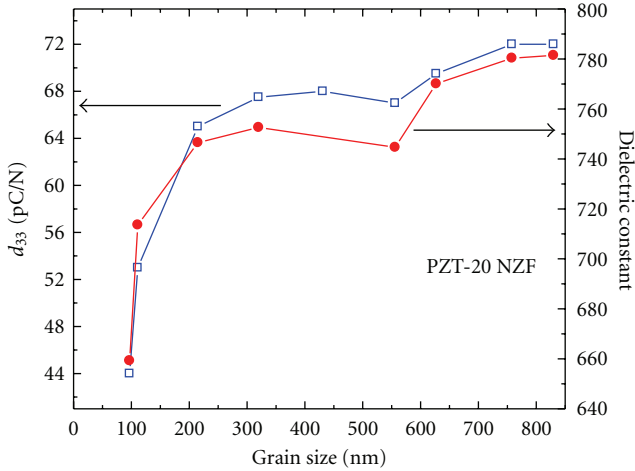
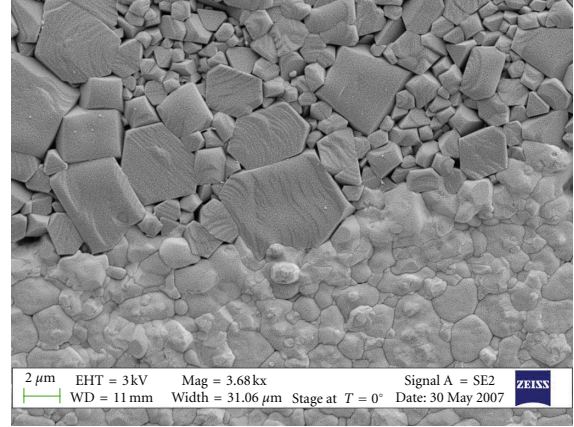
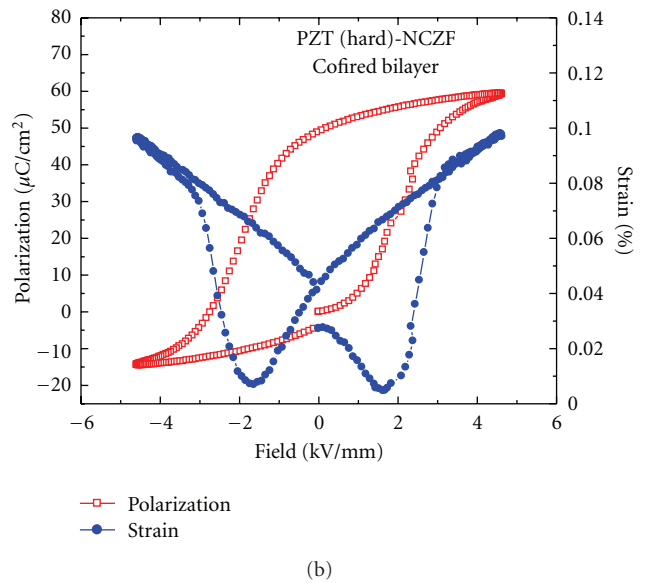


FIGURE 8: Effect of ferroelectric grain size on the piezoelectric, dielectric and magnetoelectric property of PZT-20 NZF composite.

ceramics. CuO is a common liquid-phase sintering agent in that case. The composite of this low temperature melting phase and CuFe_2O_4 phase may be associated with the transitions observed in the PZT-NCZF composites though more careful studies using high-temperature X-ray diffraction are required to confirm this hypothesis. The magnetization versus temperature behavior for bilayer composites can be resolved as summation of two curves, shown by different colored dashed line in Figure 10(b). CuFe_2O_4 has a Curie temperature of 743 K [78] and the dashed line (dark blue) indicates the Curie temperature of around 720–730 K. The second line (light blue) corresponds to the $(\text{Ni,Zn})\text{Fe}_2\text{O}_4$, which has a Curie temperature of about ~640K. This value approximately corresponds to the curie temperature of $\text{Ni}_{0.65}\text{Zn}_{0.35}\text{Fe}_2\text{O}_4$ [79]. Thus, the overall magnetic response is average of the individual contributions from CuFe_2O_4 and $\text{Ni}_{0.65}\text{Zn}_{0.35}\text{Fe}_2\text{O}_4$ proportional to the volume fraction.



(a)



(b)

FIGURE 9: SEM images of PZT (hard)-NCZF bilayer composite and its magnetoelectric response.

It was found that in T-T mode maximum magnetoelectric coefficient of around 200 mV/cm·Oe was found in bilayer composite, more than 60% enhancement in the sensitivity. The enhancement can be explained due to the improved ferroelectric and piezoelectric property of the composite.

18. Effect of Annealing and Aging

Optimized post sinter thermal treatments can be done by annealing the composites at 800°C for 10hrs, followed by quenching in air and subsequent aging at 300°C for 5 hours. It was found on annealing and aging that (i) size and density of NFM phase reduced; (ii) PZT lattice constant expanded from ($a = 3.87 \text{ \AA}$, $c = 4.07 \text{ \AA}$) to ($a = 4.07 \text{ \AA}$, $c = 4.09 \text{ \AA}$); (iii) the ferroelectric and ferromagnetic Curie temperatures decreased by 8°C and 33°C, respectively; (iv) the magnetoelectric coefficient increased by ~50%. During annealing as the structure finds more time to reduce the defects, sharp grain boundaries were observed.

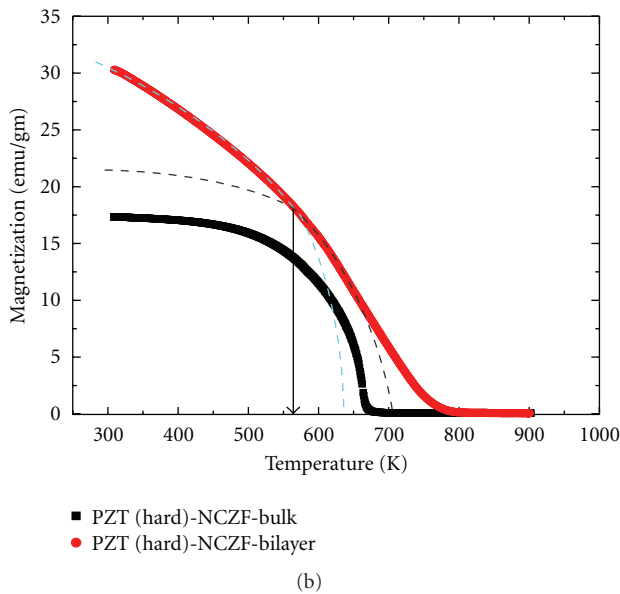
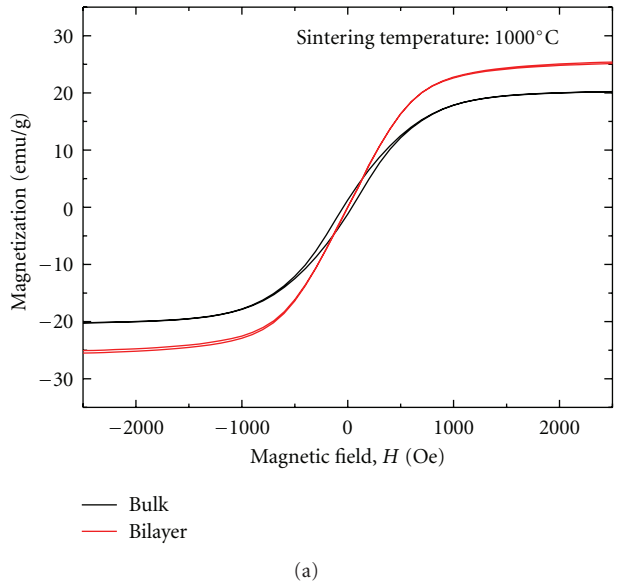
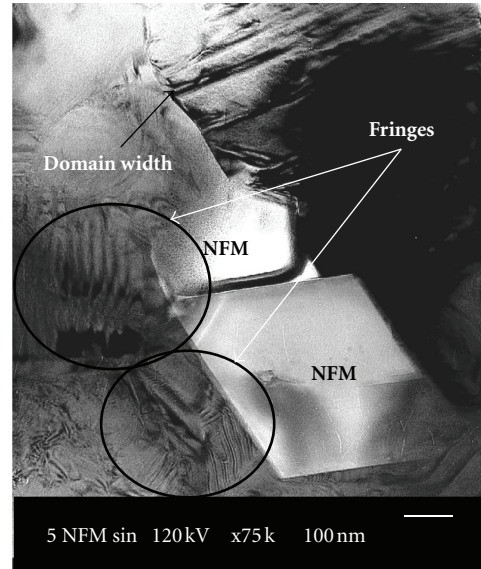
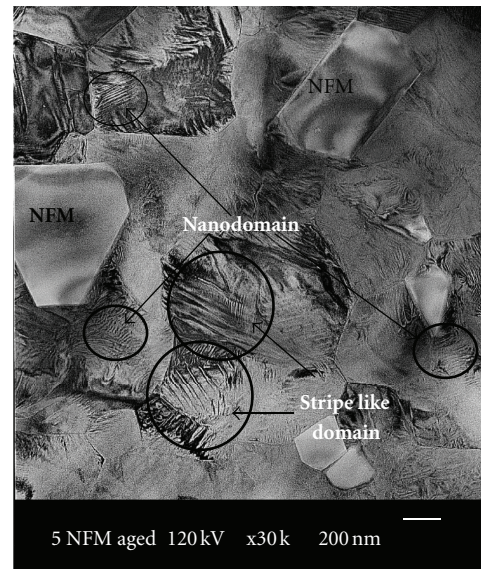


FIGURE 10: Ferromagnetic property of two types of composite. (a) Moment versus Field (hysteresis loop). (b) Magnetization as a function of temperature.

The sintered samples were found to consist of high misfit strain fields near the PZT/NFM interface which develop to accommodate the mismatch in the PZT and NFM lattice as shown by the bright field TEM images in Figure 11(a). The domain patterns had larger width characteristic of 90° domains and there is intergranular heterogeneity in domain width. The image (Figure 11(b)) after the aging process shows significantly reduced strains. The domain structure has stripe-like morphology and extend from grain boundary to grain boundary. A finer scale domain structure is also observed to exist within larger domain patterns. This finer domain pattern has striation-like morphology and is periodically spaced. Figures 12(a) and 12(b) show the dielectric constant and magnetization as a function



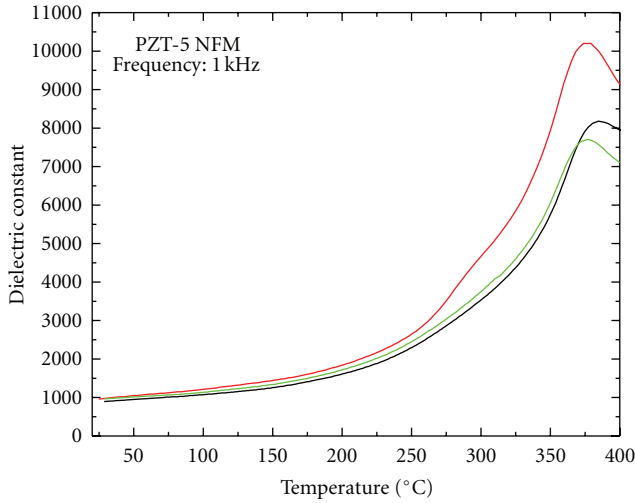
(a)



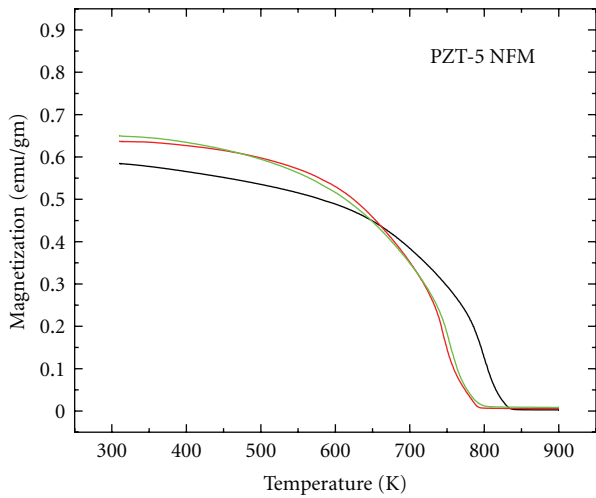
(b)

FIGURE 11: Bright-field TEM image of PZT-5 NFM composite. (a) After sintering, (b) after annealing and aging.

of temperature for a PZT-5 at% NFM composite. Data are shown in each figure for the three different thermal conditions. The ferroelectric Curie temperature, as identified by the temperature of the maximum in the dielectric constant, was only decreased slightly ($\sim 8^\circ\text{C}$) by annealing and aging. However, the ferromagnetic one was decreased notably more: from 828 K in the as-sintered condition, to 788 K after annealing. In addition, it should be noted that the saturation magnetization at room temperature was increased from about 0.58 emu/gm to 0.64 emu/gm after annealing. This modest change in magnetization after annealing at 800°C may be related to an Mn valence change in the ferrite phase. Previously, it has been shown that $\text{Mn}^{+3} \rightarrow \text{Mn}^{+2}$



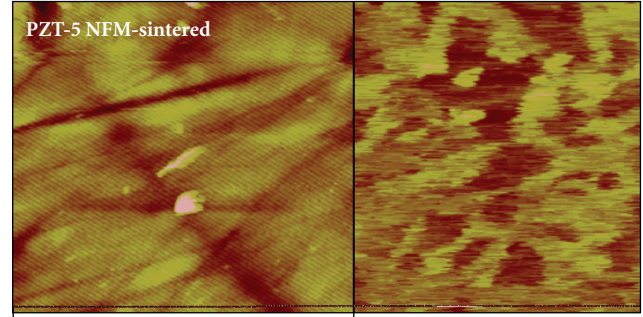
— Sintered
 — Sintered and annealed
 — Sintered, annealed and aged
 (a)



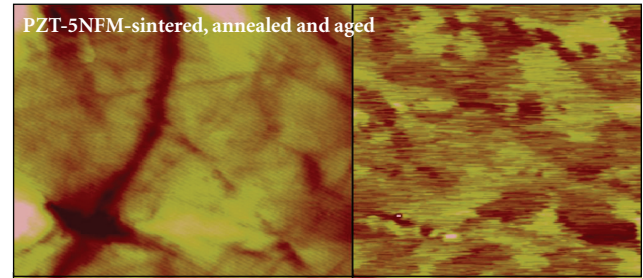
— Sintered
 — Sintered and annealed
 — Sintered, annealed and aged
 (b)

FIGURE 12: Temperature-dependent ferroelectric and ferromagnetic property of PZT-5 NFM composite. Temperature dependent, (a) dielectric constant, (b) saturation magnetization.

begins to occur for temperatures above 700°C [80], resulting in an adjustment in the stoichiometry of the ferrite phase to $[\text{Ni}(\text{Mn})_y]\text{Fe}_{1.9}\text{Mn}_{(0.1-y)}\text{O}_4$, where y is the concentration of Mn^{2+} . On quenching, this adjusted stoichiometry will be metastably frozen-in to room temperature. Since Mn^{2+} has a higher magnetic moment than Mn^{3+} , it is reasonable to expect a slight increase in saturation magnetization after annealing. ME coefficient of PZT-10 NFM was increased from 60mV/cm·Oe to 88mV/cm·Oe by annealing and aging: nearly a 50% increase. We attribute this increase is due to the expansion of lattice constant in PZT phase and reduction



(a)



(b)

FIGURE 13: PFM images of PZT-5 NFM after (a) sintering, (b) annealing/aging.

of defects at that interphase interfaces after annealing. Figures 13(a) and 13(b) compare the Piezo Force Microscopy images of the sintered and aged PZT-5NFM samples. It was found that in the sintered condition NFM phases are not homogenized as they are concentrated in one part. On the other hand in the aged condition, they are homogenized over the entire microstructure. Assuming that spinel phase is single domain, it can be hypothesized that the annealing and aging treatment results in redistribution of the magnetic phase.

The research on sintered composites has shown that cofiring multiple layers can provide higher ME coefficients. However, the drawback is that tape-casting process for synthesizing multilayers of heterogeneous materials is complex. Further, in order to improve the property of the sintered ME composites, the other variables such as composition, microstructure, geometry, texture, and postsinter heat treatment need to be optimized. As mentioned earlier, soft piezoelectric phase (high dielectric and piezoelectric constant), soft magnetic phase (high permeability and low coercivity) [81], large piezoelectric grain size ($>1\ \mu\text{m}$) [82], layered structure (bilayer/trilayer) [83], and postsintering thermal treatment (annealing and aging) [84] improve the magnetoelectric property. In order to combine all the parameters together, the challenge is to develop a unique fabrication process, in which layers of piezoelectric and magnetostrictive can be cofired together. Moreover, the poling process of

the piezoelectric phase requires high resistivity and thus electrodes have to be preserved during sintering.

19. Composite Synthesis

It was found that pressure-assisted sintering can produce trilayer composites with desired dimensions. Further, we designed the compositions such that sintering can be done at low temperatures of 900°C which resulted in stable electrodes. Powders of 0.9 Pb (Zr_{0.52}Ti_{0.48})O₃-0.1 Pb (Zn_{1/3}Nb_{2/3})O₃ [0.9 PZT-0.1 PZN] and Ni_{0.6}Cu_{0.2}Zn_{0.2}Fe₂O₄ [NCZF] were synthesized using conventional mixed oxide method. To fabricate a trilayer sample, at first a layer of NCZF powder (no binder was used) was pressed uniaxially at 52 MPa pressure inside a hardened steel die of diameter 12.5 mm and then Ag-Pd (DuPont 6160 conductor paste) electrode was printed. The second layer of 0.9 PZT-0.1 PZN was pressed on top of Ag-Pd under 5 MPa pressure inside the same die and then the electrode was again applied. The third and the final layer of NCZF layer was pressed on top of the second electrode layer. The five-layer structure NCZF/Ag-Pd/PZT-PZN/Ag-Pd/NCZF was then pressed under 20 MPa followed by using cold isostatic press (CIP) under 207 MPa. Trilayer composite was synthesized by sandwiching piezoelectric phase between magnetostrictive phases. The pressed pellet was dried at 100°C for 10 minutes and then placed inside a Lyndberg BlueM furnace by keeping 450 gm of load on top of it. The sintering was done at 900°C under a pressure of 30 kPa with very slow heating and cooling rate (~1°C/min). The sintered trilayer sample had dimensions of 3.25 mm in thickness and 11 mm in diameter. Annealing was done after sintering at 800°C for 10 hours under load. In order to polarize the samples, Ag-Pd electrode (DuPont 7714 conductor paste) was applied on top and bottom of the sample. The top electrode layer of the composite was then connected to the top of the PZT. Similarly, bottom electrode of the composite was connected to the bottom electrode of the PZT using the same Ag-Pd electrode. The poling was done at 110°C for 20 minutes under 2.2 kV/mm electric field. Microstructural analysis of the sintered samples was done by using Zeiss Leo Smart SEM on polished and thermally etched samples. Dielectric

constant measurements were performed using an HP 4284 LCR meter; and the ME voltage coefficient by lock-in amplifier method. Figure 14(a) shows the low magnification SEM image of the sintered sample. The interface electrode layers are 10 μm thick, center layer is 0.9PZT-0.1 PZN, whereas outside layers are NCZF. There were some micro- and macrocracks noticed during the sintering which could be related to the thermal mismatch between these three layers and insufficient homogenization. Figure 14(b) shows the magnified view of the interface. The microstructure is dense in both the phases with excellent adherence with the Ag-Pd electrode. Figures 14(c) and 14(d) shows the low magnification image and interface microstructure of the annealed samples. The annealing treatment resulted in the homogenization at the interface reducing the porosity and microcrack density. The macrocracks were still present in the structure. Figures 14(e) and 14(f) show the high magnification grain structure of the sintered 0.9 PZT-0.1 PZN and NCZF. The grain size observed in 0.9 PZT-0.1 PZN was more than 1 μm and that in NCZF in the range of 3–5 μm.

A significant increase in piezoelectric and dielectric properties was observed after annealing which is consistent with our previous results. The magnitude of the electromechanical coefficients d_{33} , g_{33} , ϵ_r/ϵ_o increased from 204 pC/N, 20.4×10^{-3} V-m/N, and 1132 to 250 pC/N, 22.4×10^{-3} V-m/N, and 1257. The magnitude of the loss factor (tanδ) decreased from 5.08% to 3.45% at room temperature. The loss factor increased sharply at high temperature which could be related to space charge polarization. At 100 kHz, the Curie temperature observed was around 330°C. From the resonance spectrum, it was found that the spectrum for annealed sample had less spurious and lower impedance at the resonance indicating high mechanical quality factor.

Figure 15 shows the magnetoelectric behavior of trilayer composite. The magnitude of the ME coefficient for sintered sample was of the order of 412 mV/cm·Oe with saturation field near 400 Oe. Annealed samples showed improved ME coefficient of 494 mV/cm·Oe about 20% higher than sintered ones. This magnitude is quite high from that previously reported for sintered composites. Srinivasan et. al. have derived the transverse ME coefficient for the layered composite as follows [25]:

$$\frac{\delta E_3}{\delta H_1} = \frac{-2d_{31}^p q_{11}^m v^m}{(s_{11}^m + s_{12}^m)\epsilon_{33}^{T,P} v^p + (s_{11}^p + s_{12}^p)\epsilon_{33}^{T,P} v^m - 2(d_{31}^p)^2 v_m}, \quad (32)$$

$$\frac{\delta E_3}{\delta H_1} = \frac{-2d_{31}^p q_{11}^m (t_m/(t_m + t_p))}{(s_{11}^m + s_{12}^m)\epsilon_{33}^{T,P} (t_p/t_m + t_p) + (s_{11}^p + s_{12}^p)\epsilon_{33}^{T,P} (t_m/t_m + t_p) - 2(d_{31}^p)^2 (t_m/t_m + t_p)}, \quad (33)$$

where d_{31}^p is the piezoelectric coefficient, v^m and v^p are the volume of magnetic and piezoelectric phase, t^m and t^p are the thickness of magnetic and piezoelectric phase, s_{11}^p, s_{12}^p are the elastic compliances for piezoelectric phase, s_{11}^m, s_{12}^m are the elastic compliances for magnetostrictive phase, q_{11} is the piezomagnetic coefficient of the magnetic phase, and $\epsilon_{33}^{T,P}$ is

the permittivity of the piezoelectric phase. For a radial mode disk, s_{11}^p can be calculated as follows:

$$s_{11}^p = \frac{\eta_1^2}{\rho(2\pi f_s a)^2 [1 - (\sigma^p)^2]}, \quad (34)$$

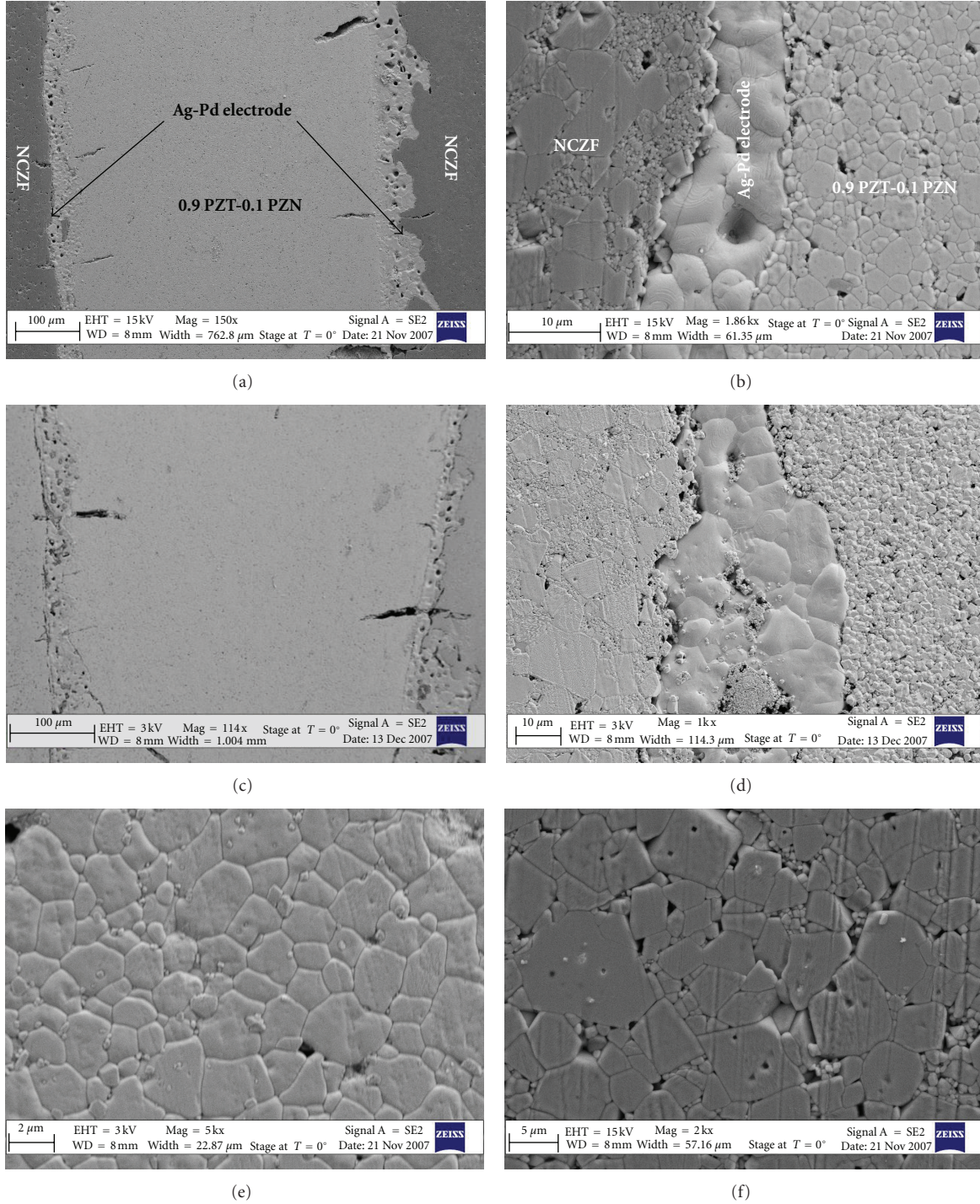


FIGURE 14: SEM micrographs. (a) low magnification image of sintered trilayer sample, (b) interface microstructure, (c) low magnification image of sintered and annealed sample, (d) interface microstructure of sintered and annealed trilayer sample, (e) grain structure of PZT side and (f) grain structure of NZF side.

where η_1 is the frequency constant, σ^p is the planar Poisson's ratio, f_s is the resonance frequency, a is the radius, and ρ is the density (~ 7.52 gm/cc). The coefficients η_1 and σ^p can be found by measuring ratio of first overtone (~ 670 kHz for sintered samples) to fundamental resonance frequency (258 kHz) [26]. For the ratio of $2.602 \eta_1$ and σ^p values were found to be 2.074 and 0.341, respectively, from IEEE

standards. Using these values s_{11}^p can be calculated as 8.66×10^{-12} m²/N. The transverse mode coupling constant k_{31} can be calculated by using the following expression [26]:

$$k_{31}^2 = k_p^2 \frac{(1 - \sigma_p)}{2}. \quad (35)$$

TABLE 1: Comparison between bulk, bilayer and trilayer ME composite

Composite	Geometry	Lattice constant	ME coefficient	DC bias
Bulk		PZT (3.87 Å, c = 4.07 Å) and NFM = 8.42 Å	110 mV/cm·Oe for PZT-20 NZF	900 Oe (T-T) mode
Bilayer			200 mV/cm·Oe	800-900 Oe (T-T) mode
Trilayer		PZT (4.04 Å, c = 4.11 Å) and NCZF = 8.41 Å	526 mV/cm·Oe (single layer PZT) And 787 mV/cm·Oe (multilayer PZT)	400 Oe(L-T) mode

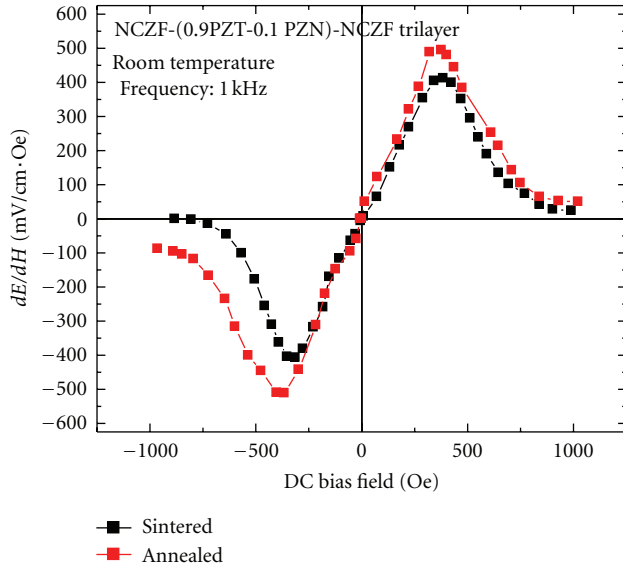


FIGURE 15: Magnetolectric coefficient as a function of dc bias field.

The values of planar coupling constant k_p are listed in Table 1. Using these values, the magnitude of k_{31} is found to be 8.03%. If k_{31} and s_{11}^E are known, then d_{31} can be calculated as follows:

$$k_{31}^2 = \frac{d_{31}^2}{(s_{11}^E \epsilon_{33}^T)}. \quad (36)$$

In order to experimentally investigate the effect of thickness ratio and achieve a higher magnetolectric coefficient, composites of different [0.9 PZT-0.1 PZN] thicknesses were synthesized. NCZF composition was used as the magnetostrictive layer and 0.9 PZT-0.1 PZN composition was used as piezoelectric layer. The amount of NCZF was fixed at 0.7 gm for top and bottom layer whereas the weight of 0.9PZT-0.1 PZN was varied from 0.8 to

The magnitude of d_{31} was found to be as 23.66×10^{-12} C/N. The magnitude of s_{12}^E was found to be -2.96×10^{-12} m²/N using the following expression [2]:

$$k_p^2 = \frac{2d_{31}^2}{[(s_{11}^E + s_{12}^E)\epsilon_{33}^T]}. \quad (37)$$

Using the values of s_{11}^m, s_{12}^m as 6.5×10^{-12} m²/N and -2.4×10^{-12} m²/N [25], q_{11} as -65×10^{-9} /Oe (at 400 Oe field), $t_m/(t_m + t_p)$ and $t_p/(t_m + t_p)$ as 0.7 and 0.3, respectively, the magnitude of the ME coefficient computed from (33) was found to be 437.1 mV/cm.Oe. This calculated value is close to the experimentally measured value of 412 mV/cm.Oe. The calculated magnitude of the ME coefficient for the annealed samples was of the order of 468 mV/cm.Oe.

20. Effect of Thickness

The thickness ratio plays an important role in the trilayer geometry. From the expression for magnetolectric coefficient for layered structure, it can be found that the magnetolectric coefficient depends on piezoelectric coefficient (d_{31}), permittivity (ϵ_{33}), elastic compliance (s_{11} and s_{12}), thickness (t_p) of the piezoelectric phase, piezomagnetic coefficient (q_{11}), elastic compliance (s_{11} and s_{12}), and thickness (t_m) of the magnetic phase. Thus (33) can be rewritten as

$$\frac{\delta E_3}{\delta H_1} = \frac{-2d_{31}^p q_{11}^m (t_m/t_p)}{(s_{11}^m + s_{12}^m)\epsilon_{33}^{T,P} + (s_{12}^p + s_{12}^p)\epsilon_{33}^{T,P} (t_m/t_p) - 2(d_{31}^p)^2 (t_m/t_p)} \quad (38)$$

0.3 gm. The interface electrode used was Dupont 6160 Ag-Pd conductor paste. The sintering was done at 900°C for 3 hrs using a load of 450 gm which is equivalent to 50 kPa. After sintering, each composite were cross-sectioned and polished for scanning electron microscopy. Figure 16 shows the cross sections of composites of PZT thickness of 0.45 and 1.2 mm, respectively. The thickness of interface electrode observed in these composites was in the range of

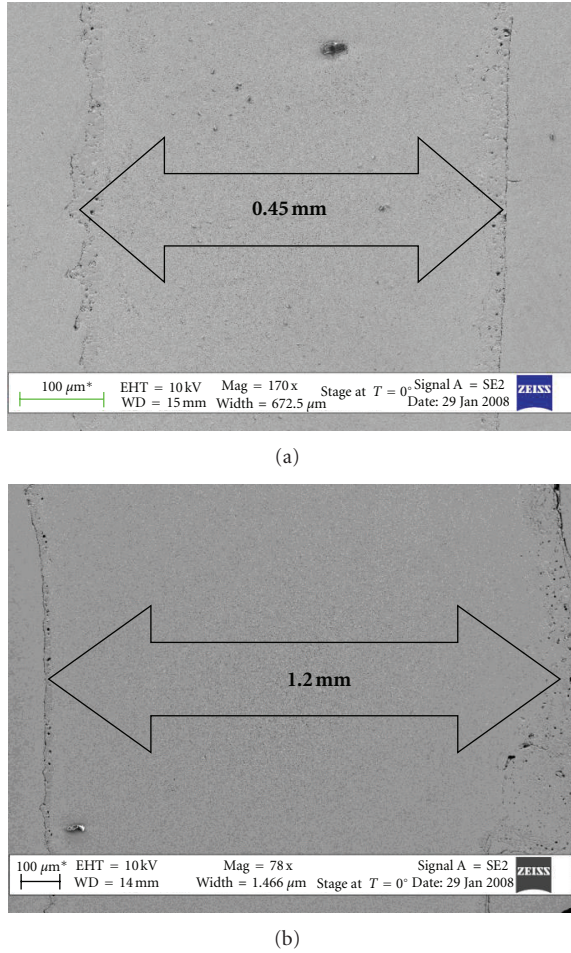


FIGURE 16: Composite of different thicknesses, (a) 0.45 mm, and (b) 1.2 mm.

5–10 μm . The adherence of the interface electrode with [0.9 PZ-0.1 PZN] and NCZF was found to be good. The [0.9 PZT-0.1 PZN] grain size observed in all the composites was above 1 μm . All the composites show piezoelectric charge constant above 225 pC/N, dielectric constant above 1150, and dielectric loss of 3–5%. X-ray elemental analysis was performed using the scanning electron microscope in order to identify any elemental diffusion through the electroded interface. The elemental analysis of Pb, Fe, and Ag shows a strong concentration of Pb was found on the [0.9 PZT-0.1 PZN] side and Fe on the NCZF side. Ag was found to be concentrated in the electroded area. By adding this interface electrode, the piezoelectric property was improved from 80 pC/N for cofired bilayer to 225 pC/N for trilayer composite. An improved dielectric constant and remarkable decrease in dielectric loss (from 29% to 5%) were recorded.

21. Effect of [0.9 PZT-0.1 PZN] Thickness and Orientation on ME Coefficient

Equation (38) shows the theoretical dependency of magneto-electric coefficient on the magnetostrictive to piezoelectric

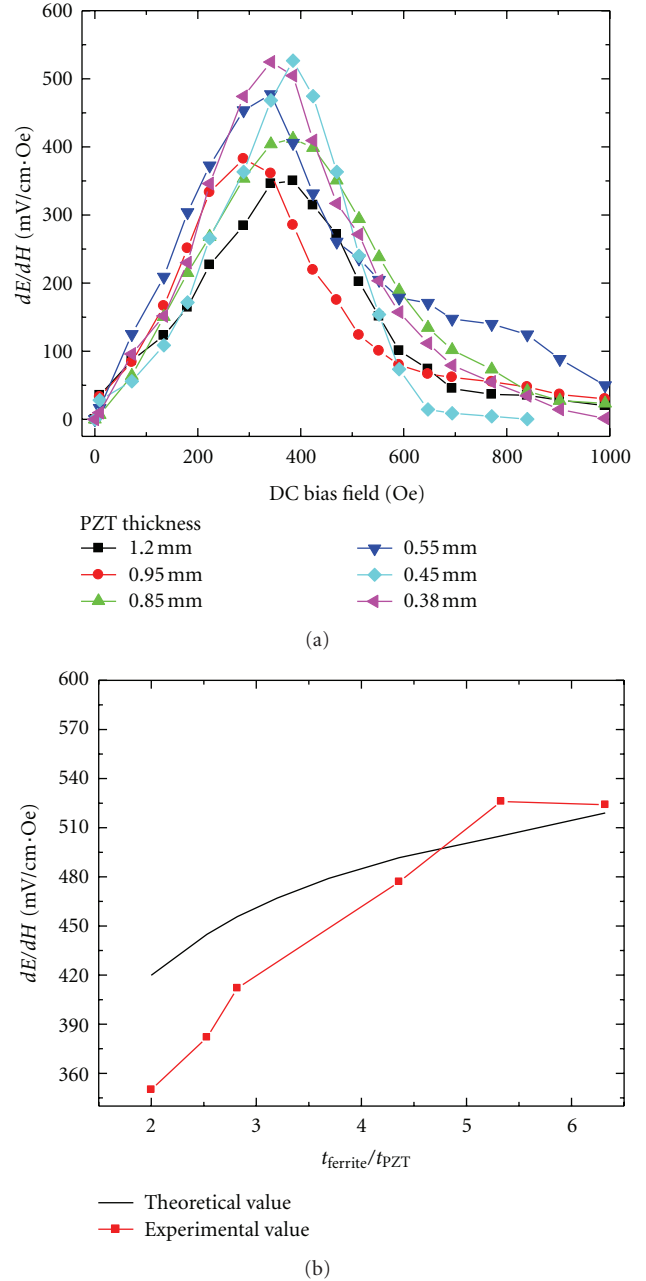


FIGURE 17: Magneto-electric coefficient as a function of DC bias field for different thickness of [0.9 PZT-0.1 PZN].

layer thickness ratio. Figure 17 shows the magneto-electric coefficient as a function of DC bias field for different thickness of [0.9 PZT-0.1 PZN]. It was found that as the thickness ratio of magnetic layer to piezoelectric layer increases (thickness of [0.9 PZT-0.1 PZN] decreases as the magnetic layer thickness was fixed), magneto-electric coefficient increases from 354 to 526 mV/cm.Oe. The maximum magneto-electric:

$$\sigma_{31f}^E = \frac{E_f E_p t_p \Delta \epsilon_0}{(1 - \gamma) (2E_f t_f + E_p t_p)}, \quad (39)$$

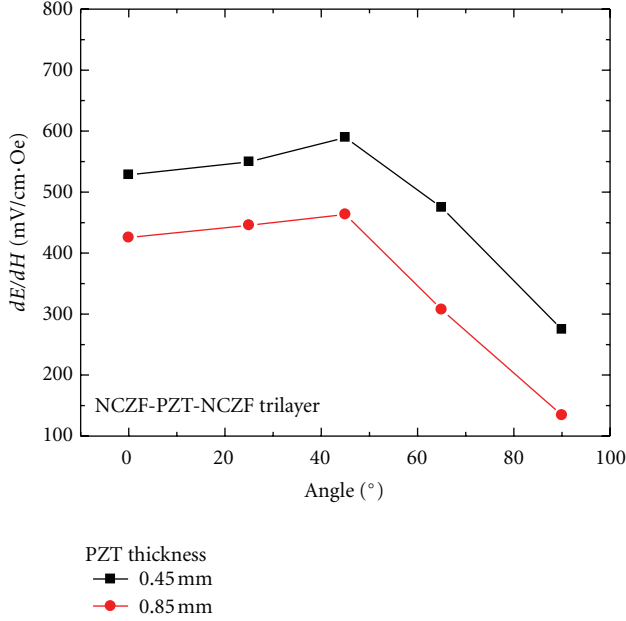


FIGURE 18: Effect of orientation on ME coefficient of NCZF-[PZT-0.1 PZN]-NCZF trilayer composite with two different [0.9 PZT-0.1 PZN] thickness.

$$\sigma_{31P}^E = -\frac{2E_f E_p t_p \Delta \epsilon_o}{(1-\gamma)(2E_f t_f + E_p t_p)}. \quad (40)$$

As the thickness of the ferrite layer remains the same (1.2 mm on top and bottom), the compressive stress on [0.9 PZT-0.1 PZN] layer can be increased if the thickness of the [0.9 PZT-0.1 PZN] layer is decreased. The compressive stress is related to magnetolectric coefficient as

$$\frac{dE}{dH} = \frac{2 \cdot g_{31} \cdot \sigma_{31P}^E}{H_{ac}}. \quad (41)$$

As the compressive stress in [0.9 PZT-0.1 PZN] is increased, magnetolectric coefficient increases.

Figure 18 shows the magnetic field (AC and DC) orientation dependence of ME coefficient for trilayer composite ([0.9 PZT-0.1 PZN] thickness = 0.45 and 0.85 mm). It was found that composite shows an increase in ME coefficient from zero degree (when magnetic field direction is parallel to the sample surface) to 45°. Maximum magnetolectric coefficient of 589 and 463 mV/cm·Oe was measured at 45°. As the angle is increased beyond 45°, the ME coefficients start to drop rapidly and when the sample surface is perpendicular to the magnetic field direction (T-T mode), a low value of 274 and 134 mV/cm·Oe was observed. It has been shown that with a real angle change, strain of the magnetic phase changes and is maximum around 51°. As the strain increases, compressive stress on [0.9 PZT-0.1 PZN] also increases which contributes to the high magnetolectric coefficient as expressed by (41). At 90° angle, the maximum magnetolectric coefficient was found to have low magnitude.

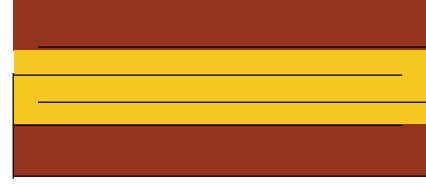


FIGURE 19: Schematic diagram for NCZF-Stack [0.9 PZT-0.1 PZN]-NCZF trilayer ME composite.

22. Effect of [0.9 PZT-0.1 PZN] Multilayering

In trilayer magnetolectric composite based on NCZF-[PZT-PZN]-NCZF, composition optimum d_{33} and dielectric constant were found to be 225 pC/N and 1150. In order to achieve higher piezoelectric and dielectric constant, it is necessary to change the electrode pattern of the [0.9 PZT-0.1 PZN] layer. In this section, the introduction of stacked [0.9 PZT-0.1 PZN] configuration in trilayer geometry will be discussed. [0.9 PZT-0.1 PZN] stacking is most common design in actuator application. This type of stack actuator design provides large coupling, fast response time, and strong force. In our trilayer ME composite, we incorporated the stacked PZT-PZN as intermediate layer between two NCZF layers.

Figure 19 shows the schematic of new trilayer design with stacked PZT-PZN. Same fabrication process was used for the synthesis of new design, but instead of single PZT-PZN layer, there were three PZT-PZN layer and interdigital electrode layer along thickness direction. The yellow layer and the black lines are identified as PZT-PZN and electrodes, respectively. To improve the sinterability of PZT-PZN, 0.5 wt% of CuO was doped. The sintering temperature and time was 900°C for 3 hours with very slow heating and cooling rate (~1°C/min). Pressure applied during sintering was 50 KPa to avoid any delamination. After sintering, the trilayer was cross-sectioned and the optical images were taken in order to measure the apparent thickness of the [0.9 PZT-0.1 PZN]. It was found that each layer of the [0.9 PZT-0.1 PZN] is around 300 μm with a combined thickness of 0.9 mm. NCZF layers were found to have thickness of 1.2 mm. Figure 20 shows the optical image of the cross-section of NCZF-stack PZT-PZN-NCZF trilayer.

The piezoelectric constant (d_{33}) increased from 204 to 535 pC/N and dielectric constant from 1132 to 5500. However, the dielectric loss of stack [0.9 PZT-0.1 PZN] increased from 5 to 13.4%, which may be due to the diffusion across the Ag-Pd electrode, which is a conductive layer. The increase in electromechanical coupling constant from 0.14 to 0.21 was observed. The impedance spectrum of the trilayer ME composite shows the resonance frequency at 523 kHz which is higher than that of single layer [0.9 PZT-0.1 PZN] which shows resonance at 258 kHz for the same dimensions. Also, the bandwidth (difference between resonance and antiresonance) was found to be higher (17 kHz) in case of trilayer composite with stack actuator configuration. Figure 21 shows the magnetolectric coefficient of stack PZT-based trilayer composite. It shows a peak coefficient of

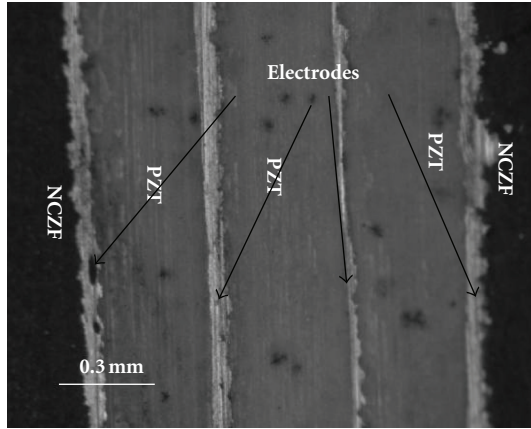


FIGURE 20: Cross sectional optical image of NCZF-Stack [0.9 PZT-0.1 PZN]-NCZF trilayer.

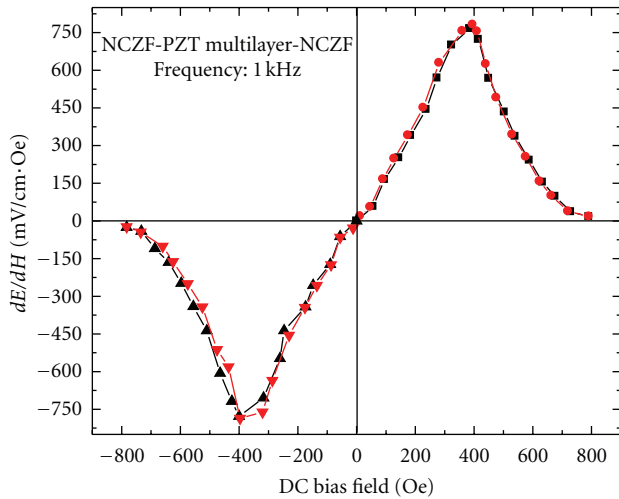
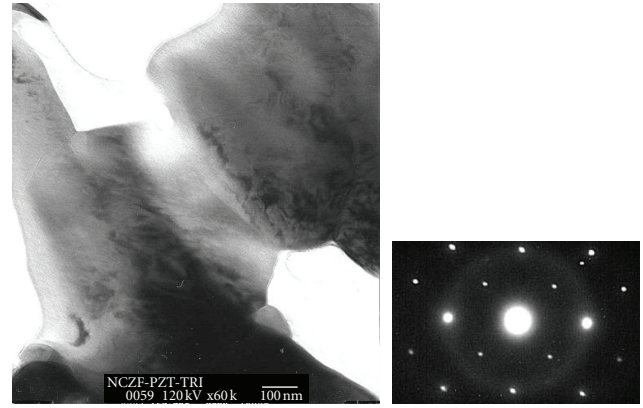


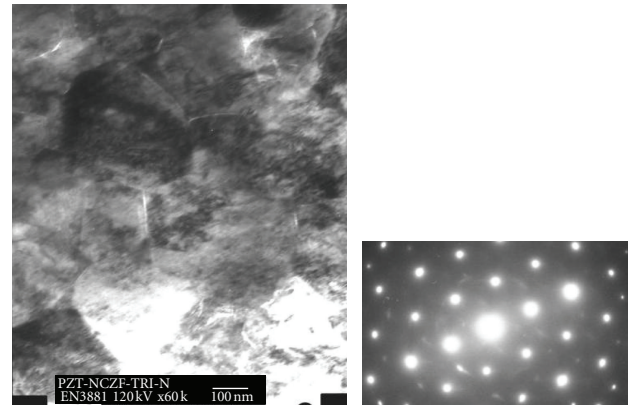
FIGURE 21: Magnetolectric coefficient of multilayer [0.9 PZT-0.1 PZN] based trilayer composite.

782 mV/cm·Oe at 400 Oe magnetic DC bias. In order to check whether there is any hysteresis behavior shown by this sample, the ME coefficient was measured from negative to positive high field and vice versa. It was found that there is very small hysteresis in the response. Compared to the single-layer PZT-PZN in trilayer configuration (412 mV/cm·Oe), stack PZT-PZN shows much higher ME coefficient.

Figures 22(a) and 22(b) show the TEM micrographs of PZT-PZN and NCZF phases close to the interface. Inset of each image shows the SAED pattern. From the diffraction pattern, pure piezoelectric and magnetic phases can be identified as there is no superlattice structure. The grain size observed was around $1 \mu\text{m}$ for piezoelectric phase and $\sim 500 \text{ nm}$ for NCZF phases. The lattice parameter was calculated to be $a = 4.04$ and $c = 4.11 \text{ \AA}$ with tetragonality (c/a ratio) of 1.017. Lattice constant for NCZF was calculated as 8.41 \AA . The micrographs were taken within $10 \mu\text{m}$ from the interface on both sides. Table 1 compares the geometry,



(a)



(b)

FIGURE 22: TEM micrograph and SAED pattern for (a) PZT-PZN and (b) NCZF near the interface.

lattice constant, ME coefficient, and DC bias field of bulk, bilayer, and trilayer composite. For bulk composite PZT, lattice constant was analyzed as strained by NFM lattice phase whereas for trilayer, the lattice constant was close to the pure phase. This clearly signifies that the interface diffusion did not take place in the trilayer which was evident in bulk and bilayer composites. The interface diffusion observed in the bilayer composite was around $30 \mu\text{m}$. Trilayer geometry with interface electrode was able to reduce the interface diffusion.

23. Grain Orientation

Crystallographic texturing of piezoelectric phase can improve the piezoelectric and ferroelectric response by exploiting the anisotropy of electrical properties. Results have been reported in literature on the effect of texturing in both lead-based and lead-free materials including BaTiO_3 (BTO), $\text{Pb}(\text{Mg}_{1/3}\text{Nb}_{2/3})\text{O}_3\text{-PbTiO}_3$ (PMN-PT), $(\text{Na}_{1/2}\text{Bi}_{1/2})\text{TiO}_3\text{-BaTiO}_3$ (NBT-BT), and $(\text{K,Na})\text{NbO}_3$ (KNN) [85–88]. The goal of this study was to implement the known texturing process in heterogeneous system consisting of varying crystal structure. This will allow developing novel hybrid materials that exhibit maximum response. As a simple rule,

rhombohedral phase oriented along the $\langle 100 \rangle$ direction provides higher piezoelectric response.

Texturing can be accomplished through various processes including, hot pressing (HP), templated grain growth (TGG) [89], and reactive template grain growth (RTGG). The advantage of TGG over HP is that the process is conducted using steps similar to that of conventional ceramic processing except with added seed material. Hence, in this study, TGG technique was adopted to synthesize the textured ME composite. The texturing process consists of two important steps: (i) seed fabrication, and (ii) seed alignment in the matrix [90]. To fabricate the seed (template), molten salt synthesis technique was utilized. It is desirable to have the seed crystal of same crystal structure as that of matrix. In this respect, BTO was chosen as the seed material since it can be grown in large size using Remeika process [91]. This synthesis process consists of heating the raw materials (BTO covered with KF salt in Pt crucible) in the temperature range of $1150\text{--}1225^\circ\text{C}$ ($\pm 5^\circ$) for 8–12 hrs and then slowly cooling down to room temperature. The crystals were separated from KF salt by hot water. The size of synthesized BTO seed was found to be in the range of $75\text{--}200\ \mu\text{m}$. Some seeds were found to be as large as 2–3 mm plates. The optical images of BTO seed fabricated using Remeika method reveals facets at the surface which could be related to the twins. A high magnification optical image (inset) shows these facets of single crystal cover the whole surface. X-ray diffraction pattern of seed indicates strong intensity peak at 22.2° which was indexed as (001) peak of perovskite BTO.

The seed crystals were used as templates for texturing piezoelectric phase in the trilayer ME composite. For this purpose, small amount (1–5 wt.%) of seed was mixed with the piezoelectric powder $0.85\text{Pb}(\text{Zr}_{0.52}\text{Ti}_{0.48})\text{O}_3\text{--}0.15\text{Pb}(\text{Zn}_{1/3}\text{Nb}_{2/3})\text{O}_3$ (PZT-PZN). The seeded powder was mixed thoroughly and dried. Trilayer was pressed with $\text{Ni}_{0.6}\text{Cu}_{0.2}\text{Zn}_{0.2}\text{Fe}_2\text{O}_4$ (NCZF) top and bottom layer and seeded PZT-15% PZN in the middle. The sample was kept for sintering in an air atmosphere for 50 hr soaking time so that the grains can grow along the preferred orientation of seed crystal. A bilayer sample was also synthesized in order to study the structural characteristics of piezoelectric layer.

Figure 23 shows the X-ray diffraction pattern of the synthesized sample which shows considerable increase in (001)/(100), (111), (002)/(200) peak intensities compared to the (110)/(101) peak. Also, the peak splitting was clearly observed in (001)/(100) and (002)/(200) peaks, which indicates the increase in tetragonality. From this pattern, the lattice parameter can be calculated to be $a = 4.008\ \text{\AA}$, and $c = 4.098\ \text{\AA}$ and the c/a ratio can be calculated as 1.022. Figure 23 also compares the XRD pattern of textured PZT-PZN with randomly oriented PZT-PZN. From X-ray diffraction patterns, the degree of texturing was calculated by Lotgering method [20] given as

$$f_{00l} = \frac{P_{00l} - P_0}{1 - P_0}, \quad (42)$$

where $P_{00l} = (\sum I_{00l})/(\sum I_{hkl})$ and $P_0 = (\sum I^0_{00l})/(\sum I^0_{hkl})$ where I_{hkl} and I^0_{hkl} are the intensities of hkl plane

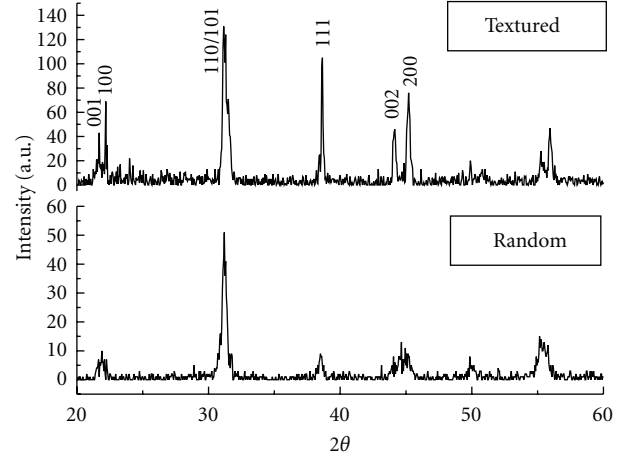


FIGURE 23: X-ray diffraction pattern of textured PZT-PZN compared to randomly oriented PZT-PZN.

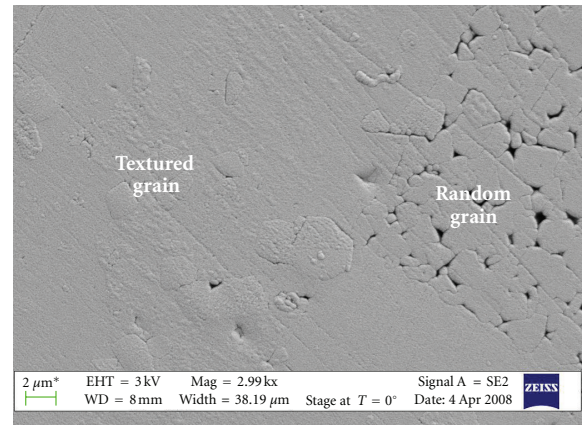


FIGURE 24: High-magnification SEM micrograph of PZT-PZN showing textured grain and randomly oriented grain interface.

for the textured and random sample and $\sum I_{00l}$ is the summation of the intensities of all 001 planes. Using this formula, the Lotgering factor was calculated to be $f = 0.35$ for samples textured along (001) direction. Figure 24 shows the presence of very large grains which were considered to be as textured grains with average size in the range of $200\text{--}350\ \mu\text{m}$ as compared to $1\text{--}2\ \mu\text{m}$ grain size for surrounding grains. The grain size observed in Figure 24 is very high due to large soaking period of 50 hrs.

These are preliminary results related to our texturing are promising and more in-depth study is required to confirm the orientation and degree of texturing. The cross-section revealed by optical microscopy shows crack free interfaces with intact electrode layer. PZT-PZN layer was found to be around $0.5 \pm 0.02\ \text{mm}$ in thickness and NCZF thickness was of the order of $1.2 \pm 0.05\ \text{mm}$. The samples were poled at 120°C for 20 minutes under a field of $2.5\ \text{kV/mm}$ in a silicone oil bath. The longitudinal piezoelectric constant (d_{33}) was measured to be $325 \pm 10\ \text{pC/N}$ with dielectric constant of 1865 ± 30 and loss of 7% at room temperature at 1 kHz. Compared to the randomly oriented PZT-PZN

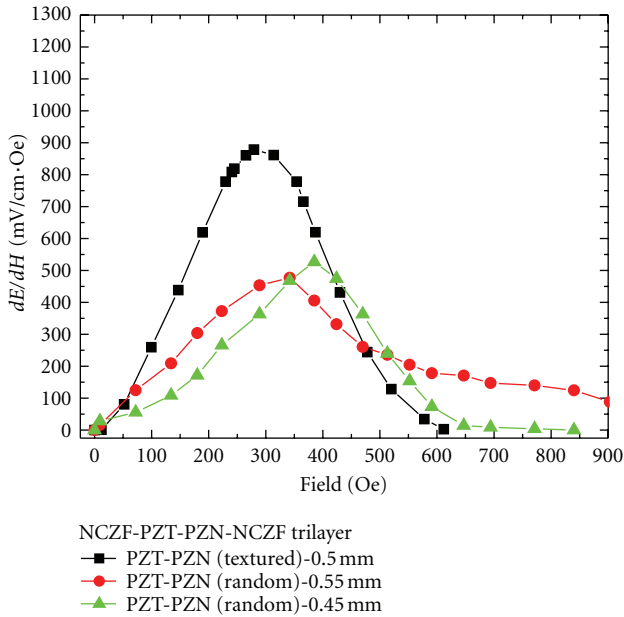


FIGURE 25: ME coefficient of partially textured trilayer composite compared with randomly oriented composite.

intermediate layer, d_{33} increases by 44% and dielectric constant increases by 50% by partial texturing. Figure 25 shows the ME coefficient of trilayer with textured PZT-PZN as function of DC bias. Three samples from each batch were measured and the average value was reported. The deviation observed from sample to sample within each batch was around 5%. The peak ME coefficient observed was around 878 ± 20 mV/cm·Oe DC bias field. For randomly oriented PZT-PZN layer, ME coefficient observed was around 526 ± 25 mV/cm·Oe for layer thickness of 0.45 mm and around 500 ± 15 mV/cm·Oe for thickness of 0.55 mm. This increase in piezoelectric and magnetoelectric coefficient in partially textured trilayer can be explained in terms of domain engineering.

24. Future of Sintered Composite

Laminate composites involve multiple step assembly process and are sensitive to the changes in configuration. Thus, our research emphasis has been on enhancing the ME coefficient in bulk sintered composites. The challenges associated with sintered composites are (i) reducing the diffusion across interface, (ii) reducing elastic softening at the interface, and (iii) reducing connectivity of the magnetostrictive phase without compromising the contact area with piezoelectric phase.

All these challenges can be addressed by synthesizing sintered composites from core-shell particles where piezoelectric phase is the core and magnetostrictive phase is the shell [2, 92]. The elastic coupling can be maximized by having coherent response from the magnetostrictive phase under dc bias such that the stress on the piezoelectric lattice

across the grains is in phase with each other. This is only possible if there is uniform distribution of the magnetostrictive phase with respect to the piezoelectric matrix. This core-shell composite has the possibility to provide effective inter-phase exchange coupling originating from the maximized inter-phase contact. Thus, we synthesized a core-shell particulate composite of $\text{Pb}(\text{Zr,Ti})\text{O}_3$ (PZT) and NiFe_2O_4 (NF), and characterized its magnetoelectric property.

PZT particles corresponding to formulation $\text{Pb}(\text{Zr}_{0.52}\text{Ti}_{0.48})\text{O}_3$ were synthesized using conventional ceramic processing route. Nano-NF particles were synthesized by chemical synthesis technique using the following processing steps. A mixture of 256 mg of $\text{Ni}(\text{acac})_2$ and 500 mg of 1,2-hexadecanediol was added to a 125 mL European flask containing a magnetic stir bar. Benzyl ether 20 mL was then transferred into the flask and the contents were stirred while purging with N_2 for 20 min at room temperature. The flask was then heated to 120°C and the temperature was held for 20 min. During this time, 0.2 mmol of $\text{Fe}(\text{CO})_5$ was injected into the flask while the N_2 purging continued. After 1 minute, 1 mL of oleic acid and 1 mL of oleylamine were injected and the mixture was maintained under N_2 blanket and heated to 160°C at a rate of 5°C per minute where it was held for 10 minutes. The flask was maintained at the refluxing temperature of 295°C for 30 min before cooling down to room temperature under the N_2 blanket. Size of NiFe_2O_4 was controlled by varying the amount of surfactants and heating rates. When faster heating rate and more surfactants were used, bigger NF particles were obtained. Coating of NiFe_2O_4 nanoparticles on PZT was done using similar recipe as that for synthesizing the NF nanoparticles. PZT particles were added in the beginning of synthesis keeping the other parameters constant. Amount of PZT particles was varied from 500 mg to 2 gm in order to vary the coating thickness and obtain different ratio of NF to PZT.

Figure 26(a) shows the TEM image of nanosize NF particles. The size of the particles was found to be in the range of 20–30 nm with hexagonal shape. Figure 26(b) shows the X-ray diffraction pattern of NF nanoparticles (red) compared with that of large size particles (black), both exhibiting spinel structure. The peak broadening occurred as the particle size became smaller. Figure 26(c) shows the magnetic hysteresis loop of the NF nanoparticles. Coercive field and magnetization were found to be lower in comparison with the large size particles, as we will discuss later. From Figures 26(b) and 26(c), it can be seen that excellent structural and magnetic properties in NF nanoparticles can be achieved using the chemical synthesis method.

Figure 27(a) shows the SEM images of PZT-NF core shell structure. EDS spot analysis on these particles showed presence of both PZT and NF. Figure 27(b) shows the TEM image of PZT particle coated with NF nanoparticles. The difference in contrast was clearly observed for two different sizes of particles. TEM investigations showed that the NF nanoparticle shell over the PZT core was 2-3 layers in thickness. PZT-NF core-shell particles were sintered at low temperature of 950°C and long holding time of 5 hrs. In order to increase the resistivity, a thin layer of pure PZT was pressed as top layer in a 0.25 inch die under hydraulic

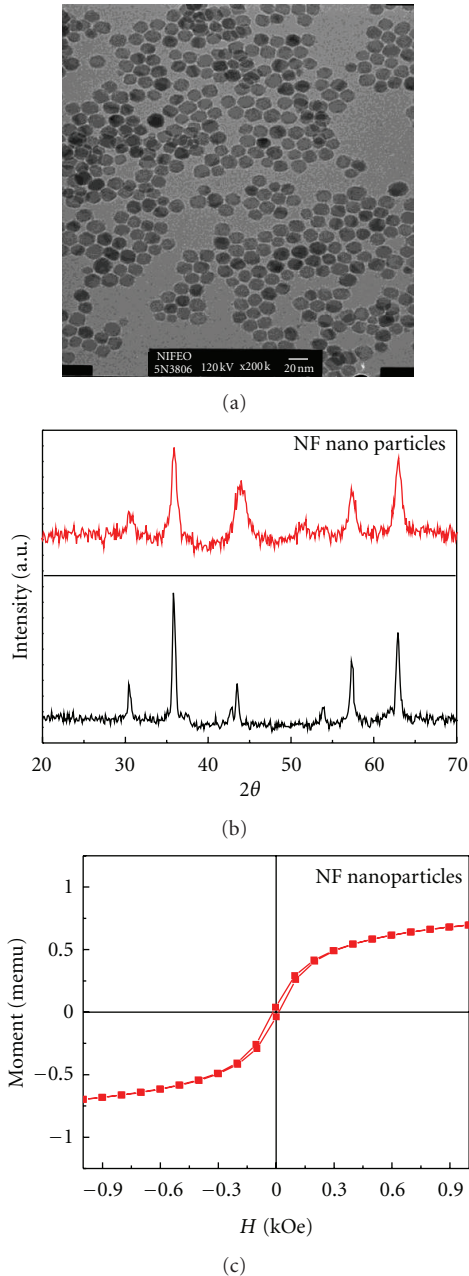


FIGURE 26: (a) TEM image, (b) X-ray diffraction pattern, and (c) magnetic properties of NF nano particles.

pressure of 2 ksi followed by cold isostatic pressure of 30 ksi. Figure 27(c) show the low magnification SEM image of PZT-NF core-shell structure. The microstructure of the sintered composite was dense with very small fraction of porosity. The grain size of the composite was found to be in the range of 500–800 nm. Inset of Figure 27(c) shows a magnified view of core-shell grains. TEM analysis revealed that the shell was present at the grain boundary of large fraction of grains. The coating thickness was equivalent to 2-3 layers, which varies from 40–70 nm. The size of nanoparticles in the shell was larger than the as-synthesized nanoparticles due to high-temperature sintering process.

Figure 27(d) shows the magnetic properties of as synthesized NF nanoparticles and PZT-NF core-shell structure. One major difference can be immediately noted in this figure related to increase in coercive field as compared to the nanoparticles. For PZT-NF core-shell particles, the coercive field was found to be 216 Oe whereas for as, synthesized nanoparticles, this magnitude was significantly lower. This may be attributed to the increase in size of the NFO shell during sintering process. As particle size decreases, coercivity decreases and for very low value of particle size ferromagnetic to superparamagnetic transition occurs [93, 94]. It has been shown in literature that with increasing particle size from 1 nm and above, the magnitude of coercive field increases and reaches maxima before dropping again with further increase in size. The particle size where maximum in coercive field occurs corresponds to the size of single-domain particle. The size of the shell in the sintered composite may be close to the single-domain particle size and hence the coercive field observed was high.

Figure 28(a) shows the TEM image of grain structure for sintered PZT-NF composite. Figure 28(b) shows the variation of magnetoelectric coefficient as a function of DC bias for the sintered composite. The composite was electroded and poled at 2.5 kV/mm for 30 minutes in silicone oil bath. The temperature was fixed at 120°C. The piezoelectric (d_{33}) and dielectric properties were measured on poled and aged sample. The composite had d_{33} of 60 pC/N, dielectric constant of 865, and dielectric loss of 5.45%. The peak ME coefficient of 195 mV/cm.Oe was observed at 454 Oe. This magnitude is much higher than that obtained for random polycrystalline-sintered composites [95]. Further, it was found that in the DC bias range of 265 to 617 Oe, the ME coefficient remained above 175 mV/cm.Oe, which is almost 90% of the peak value. This data is quite different as compared to that obtained for bulk particulates which exhibit sharp peaks. This wide bandwidth offers significant advantages for sensing applications. This may be due to the hard nature (larger coercive field) of the magnetic phase. The coercive field was of the order of 216 Oe for the core-shell structure. Above this field, the magnetization rotation contributes towards magnetostrictive strain. Above 617 Oe, the ME coefficient drops as the piezomagnetic coefficient starts to drop rapidly.

25. Conclusion

The improvement of the magnetoelectric coefficient of the sintered composite was discussed in this review along with composition-microstructure-property relationship. A new material constant n was derived from the condition for maximization of g constant ($|d| = \epsilon^n$). According to the developed model, as the magnitude of n decreases towards unity a giant enhancement in the magnitude of the g constant can be obtained. The experimental data was found to be consistent with this prediction. Effect of matrix grain size on the magnetoelectric coefficient of PZT-20 NZF particulate composites was studied. It was found that grain size has significant effect on the piezoelectric, ferroelectric, and dielectric properties of the composite and

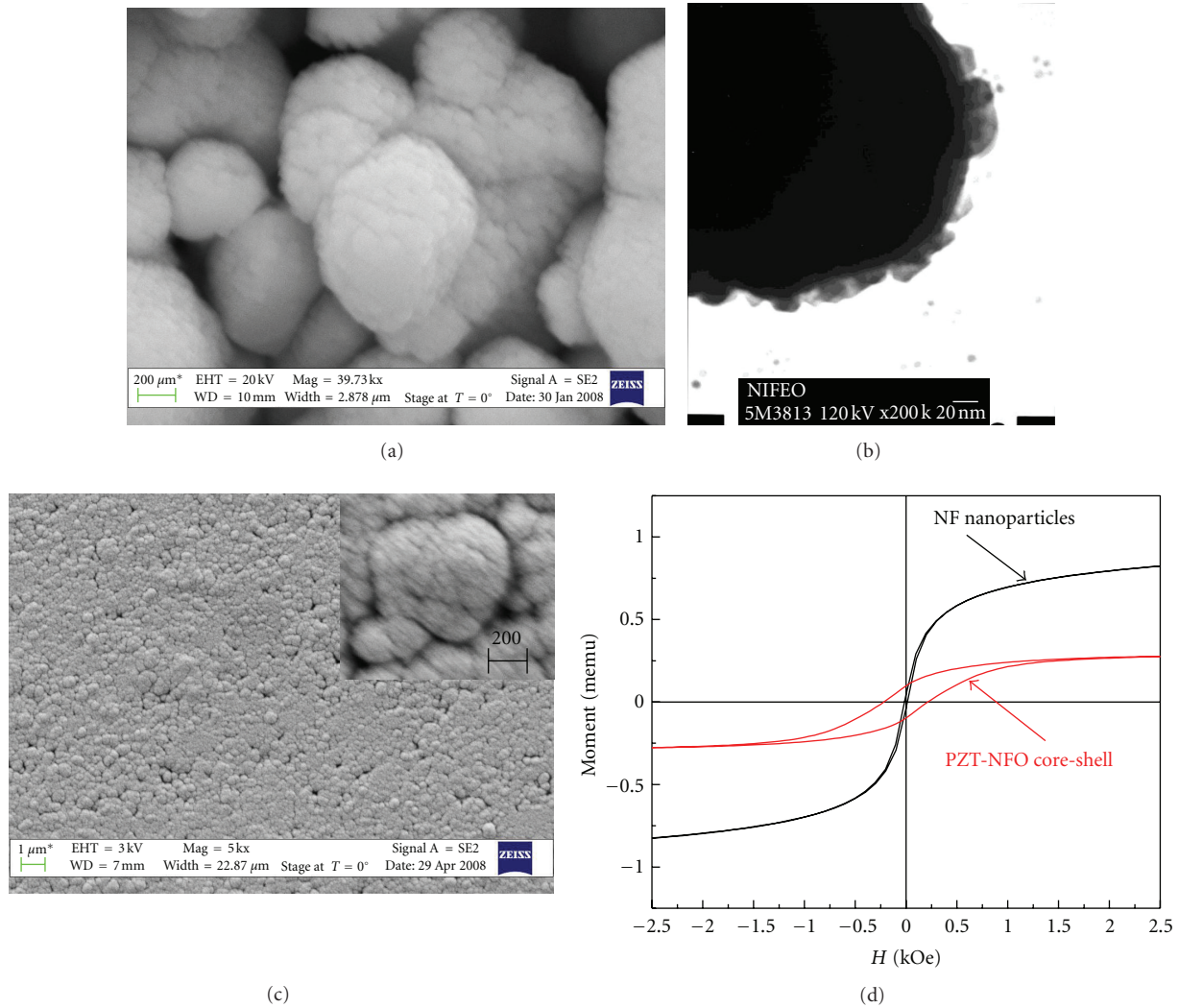
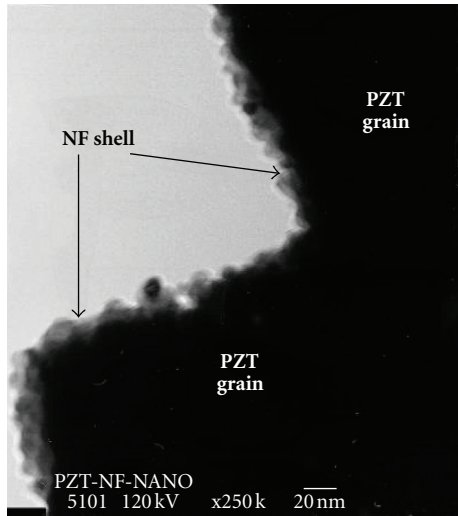


FIGURE 27: Micrographs for PZT-NF core-shell structure, (a) SEM and (b) TEM, (c) SEM microstructure of sintered PZT-NF core shell structure, and (d) comparison of magnetic hysteresis property of NF nanoparticles and PZT-NF core-shell structure.

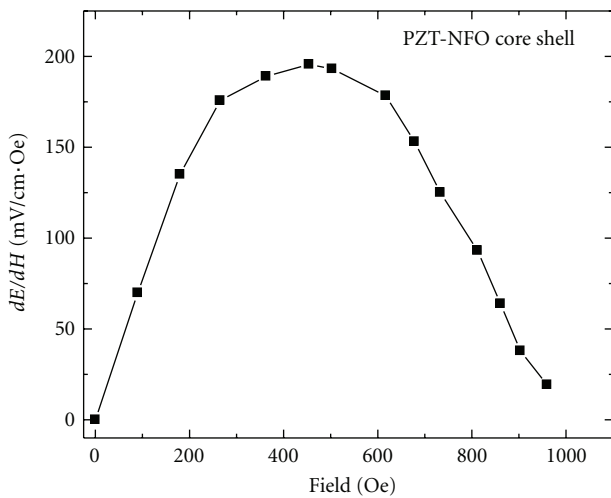
hence influences the magnetoelectric property. There is a critical grain size below which the piezoelectric charge constant (d_{33}), dielectric constant, and piezoelectric voltage constant (g_{33}) drops rapidly. This critical grain size is in the range of 100–150 nm. Above 200 nm, the piezoelectric properties increases slowly and saturates at 600 nm. Samples having grain size of around 100 nm show small magnitude of ME coefficient (54.4 mV/cm·Oe) while those with grain size of 600 nm exhibit a value of 155 mV/cm·Oe.

The effect of postsintering thermal treatment of PZT-NFM composites show that there is a correlation between structural deformation in PZT matrix, presence of defects between component phases in piezoelectric-magnetostrictive composites, and change in magnetization with changes in the ME coefficient. It was found that lattice expansion of PZT [from ($a = 3.87 \text{ \AA}$, $c = 4.07 \text{ \AA}$) to ($a = 4.07 \text{ \AA}$, $c = 4.09 \text{ \AA}$)], removal of defects, and increase in magnetization contribute to the enhancement in ME coefficient after annealing and aging. There is a decrease

in ferroelectric and ferromagnetic Curie temperatures by 8°C and 33°C and at least 50% enhancement was observed in magnetoelectric coefficient after annealing and aging. A sintering process was introduced to fabricate NCZF-(0.9 PZT-0.1 PZN)-NCZF trilayer composites. Soft piezoelectric phase with grain size of more than 1 μm, and low coercivity magnetostrictive phase with grain size of 3–5 μm were obtained with excellent adherence to Ag-Pd electrode. Sintered and annealed samples showed ME coefficient of ~412 and 494 mV/cm·Oe, respectively, which are quite large compared to the previously reported values. Optimization of magnetostrictive to piezoelectric thickness ratio showed a magnetoelectric coefficient of 525 mV/cm·Oe when the angle between the sample and the magnetic field direction is zero. A slightly higher value (595 mV/cm·Oe) was observed when the angle was changed to 45°. It was also found that when the intermediate piezoelectric layer is changed from single layer to trilayer stack geometry then piezoelectric and dielectric property of the composite improved remarkably



(a)



(b)

FIGURE 28: TEM image of sintered core-shell structure, (b) magnetoelectric coefficient as a function of DC bias field for sintered PZT-NF core shell structure.

from 204 pC/N and 1132 to 535 pC/N and 5500, respectively. This enhancement contributes to the high magnetoelectric response of 782 $\text{mV/cm}\cdot\text{Oe}$.

Texturing the piezoelectric phase inside the trilayer ME composite improved the ME coefficient. X-ray diffraction and scanning electron microscopy showed that the texturing occurred inside the piezoelectric grains by using BaTiO_3 seeds. The degree of texturing was found to be 0.35 and 0.22 for (001) and (111) direction, respectively. For this moderate texturing, improvement in piezoelectric and dielectric constant was by 40–50%. It improved the ME coefficient by 67%, from 526 $\text{mV/cm}\cdot\text{Oe}$ to 878 $\text{mV/cm}\cdot\text{Oe}$. Core shell particles of PZT and NFO were synthesized using chemical synthesis route with PZT as core and NFO as shell. The core-shell particles were sintered using compaction and annealed at 1025°C for 5 hours. The magnetic property (coercivity) of core shell particles was remarkably different than the as

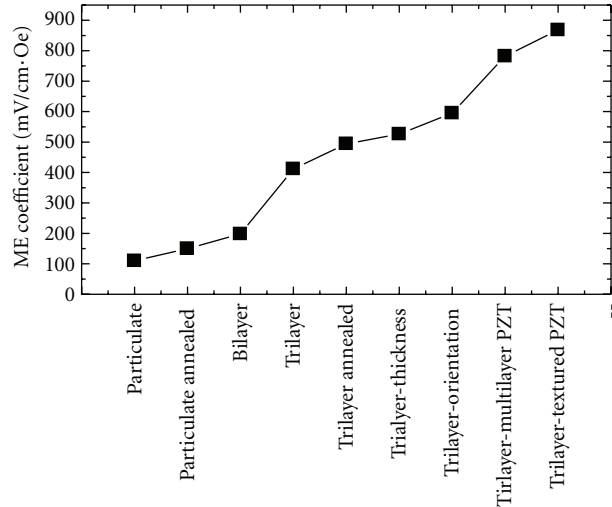


FIGURE 29: Progress in magnetoelectric sintered composite.

synthesized nanoparticles. Coercive field increased to 210 Oe, which is quite high for NFO nanoparticles. Due to this hard nature of NFO nanoparticles, high ME coefficient ($>175 \text{ mV/cm}\cdot\text{Oe}$) over the wide range of field was observed with peak ME coefficient of 195 $\text{mV/cm}\cdot\text{Oe}$.

Figure 29 shows the progress in ME-sintered composite research starting from 110 $\text{mV/cm}\cdot\text{Oe}$ to 878 $\text{mV/cm}\cdot\text{Oe}$ ~ a 700% improvement—which is a significant contribution. Also at the end it was predicted that the nano-particulate core shell assembly has the promise for achieving large ME coefficient in the sintered composites.

Acknowledgment

S. Priya would like to acknowledge the financial support from NSF INAMM Program.

References

- [1] J. Ryu, A. V. Carazo, K. Uchino, and H. E. Kim, "Piezoelectric and magnetoelectric properties of lead zirconate titanate/Ni-ferrite particulate composites," *Journal of Electroceramics*, vol. 7, no. 1, pp. 17–24, 2001.
- [2] V. C. Flores, D. B. Baques, D. C. Flores, and J. A. M. Aquino, "Enhanced magnetoelectric effect in core-shell particulate composites," *Journal of Applied Physics*, vol. 99, no. 8, Article ID 08J503, 3 pages, 2006.
- [3] T. G. Lupeiko, I. V. Lisnevskaya, M. D. Chkheidze, and B. I. Zvyagintsev, "Laminated magnetoelectric composites based on nickel ferrite and pzt materials," *Inorganic Materials*, vol. 31, no. 9, pp. 1139–1142, 1995.
- [4] M. Feibig, "Revival of the magnetoelectric effect," *Journal of Physics D*, vol. 38, pp. R123–R152, 2005.
- [5] C. Ederer and N. A. Spaldin, "Recent progress in first-principles studies of magnetoelectric multiferroics," *Current Opinion in Solid State & Materials Science*, vol. 9, pp. 128–139, 2005.
- [6] J. van Suchtelene, "Product properties: a new application of composite materials," *Philips Research Report*, vol. 27, no. 3, pp. 28–37, 1972.

- [7] G. Smolenskii and V. A. Ioffe, Colloque International du Magnetisme, Communication no. 71, 1958.
- [8] J. Wang, J. B. Neaton, H. Zheng et al., "Epitaxial BiFeO₃," *Science*, vol. 299, no. 5613, pp. 1719–1722, 2003.
- [9] J. Wang, H. Zheng, S. E. Lofland et al., "Multiferroic BaTiO₃-CoFe₂O₄ Nanostructures," *Science*, vol. 303, no. 5658, pp. 661–663, 2004.
- [10] C. Ederer and N. A. Spaldin, "A new route to magnetic ferroelectrics," *Nature Materials*, vol. 3, no. 12, pp. 849–851, 2004.
- [11] W. Eerenstein, N. D. Mathur, and J. F. Scott, "Multiferroic and magnetoelectric materials," *Nature*, vol. 442, no. 7104, pp. 759–765, 2006.
- [12] N. Hur, S. Park, P. A. Sharma, J. S. Ahn, S. Guha, and S. W. Cheong, "Electric polarization reversal and memory in a multiferroic material induced by magnetic fields," *Nature*, vol. 429, no. 6990, pp. 392–395, 2004.
- [13] C. W. Nan, M. I. Bichurin, S. Dong, D. Viehland, and G. Srinivasan, "Multiferroic magnetoelectric composites: historical perspective, status, and future directions," *Journal of Applied Physics*, vol. 103, no. 3, Article ID 031101, 35 pages, 2008.
- [14] S. Priya, R. Islam, S. Dong, and D. Viehland, "Recent advancements in magnetoelectric particulate and laminate composites," *Journal of Electroceramics*, vol. 19, no. 1, pp. 147–164, 2007.
- [15] G. R. Harshe, *Magnetoelectric effect in piezoelectric—magnetostrictive composite*, Ph.D. dissertation, Pennsylvania State University, University Park, Pa, USA, 1991.
- [16] J. F. Herbst, T. W. Capehart, and F. E. Pinkerton, "Estimating the effective magnetostriction of a composite: a simple model," *Applied Physics Letters*, vol. 70, no. 22, Article ID 3041, 3 pages, 1997.
- [17] C. W. Nan, M. Liu, X. Feng, and S. Yu, "Possible giant magnetoelectric effect of ferromagnetic rare-earth-iron-alloys-filled ferroelectric polymers," *Applied Physics Letters*, vol. 78, no. 17, Article ID 2527, 3 pages, 2001.
- [18] D. N. Astrov, "The magnetoelectric effect in antiferromagnetics," *Soviet Physics, JETP*, vol. 11, pp. 708–709, 1960.
- [19] D. N. Astrov, B. I. Al'shin, R. V. Zhorin, and L. A. Drobyshev, *Soviet Physics, JETP*, vol. 28, p. 1123, 1968.
- [20] G. Smolenskii and V. A. Ioffe, Colloque International du Magnetisme, Communication, no. 71, 1958.
- [21] T. Kimura, T. Goto, H. Shintani, K. Ishizaka, T. Arima, and Y. Tokura, "Magnetic control of ferroelectric polarization," *Nature*, vol. 426, no. 6962, pp. 55–58, 2003.
- [22] T. Lottermoser, T. Lonkai, U. Amann, D. Hohlwein, J. Ihringer, and M. Fiebig, "Magnetic phase control by an electric field," *Nature*, vol. 430, no. 6999, pp. 541–544, 2004.
- [23] B. B. Van Aken, T. T. A. Palstra, A. Filippetti, and N. A. Spaldin, "The origin of ferroelectricity in magnetoelectric YMnO₃," *Nature Materials*, vol. 3, no. 3, pp. 164–170, 2004.
- [24] M. Fiebig, T. Lottermoser, D. Fröhlich, A. V. Goltsev, and R. V. Pisarev, "Observation of coupled magnetic and electric domains," *Nature*, vol. 419, no. 6909, pp. 818–820, 2002.
- [25] M. Zeng, J. G. Wan, Y. Wang et al., "Resonance magnetoelectric effect in bulk composites of lead zirconate titanate and nickel ferrite," *Journal of Applied Physics*, vol. 95, no. 12, Article ID 8069, 5 pages, 2004.
- [26] J. Zhai, Z. Xing, S. Dong, J. Li, and D. Viehland, "Magnetoelectric laminate composites: an overview," *Journal of the American Ceramic Society*, vol. 91, no. 2, pp. 351–358, 2008.
- [27] R. E. Newnham, "Composite Electro ceramics," *Ferroelectrics*, vol. 68, no. 1–4, pp. 1–32, 1986.
- [28] T. H. Odell, "Magnetoelectrics—a new class of materials," *Electronics and Power*, vol. 11, no. 8, pp. 266–267, 1965.
- [29] R. E. Newnham, "Composite piezoelectric transducers," *Materials in Engineering*, vol. 2, no. 2, pp. 93–106, 1980.
- [30] J. V. D. Boomgaard, A. M. J. G. Van Run, and J. Van Suchtelen, "Magnetoelectricity in piezoelectric-magnetostrictive composite," *Ferroelectrics*, vol. 10, pp. 295–298, 1976.
- [31] J. V. D. Boomgaard and R. A. J. Born, "A sintered magnetoelectric composite material BaTiO₃-Ni(Co, Mn) Fe₂O₄," *Journal of Materials Science*, vol. 13, no. 7, pp. 1538–1548, 1978.
- [32] J. V. D. Van Den Boomgaard, D. R. Terrell, R. A. J. Born, and H. F. J. I. Giller, "An in situ grown eutectic magnetoelectric composite material—part I Composition and unidirectional solidification," *Journal of Materials Science*, vol. 9, no. 10, pp. 1705–1709, 1974.
- [33] A. M. J. G. Van Run, D. R. Terrell, and J. H. Scholing, "An in situ grown eutectic magnetoelectric composite material—part 2 Physical properties," *Journal of Materials Science*, vol. 9, no. 10, pp. 1710–1714, 1974.
- [34] J. Ryu, S. Priya, K. Uchino, and H.-E. Kim, "High Magnetoelectric Properties in 0.68Pb(Mg_{1/3}Nb_{2/3})O₃-0.32PbTiO₃ Single Crystal 28 and Terfenol-D Laminate Composites," *Journal of the Korean Ceramic Society*, vol. 39, pp. 813–817, 2002.
- [35] J. Ryu, S. Priya, K. Uchino, and H. E. Kim, "Magnetoelectric effect in composites of magnetostrictive and piezoelectric materials," *Journal of Electroceramics*, vol. 8, no. 2, pp. 107–119, 2002.
- [36] S. Dong, J. F. Li, and D. Viehland, "Ultrahigh magnetic field sensitivity in laminates of TERFENOL-D and Pb(Mg_{1/3}Nb_{2/3})O₃-PbTiO₃ crystals," *Applied Physics Letters*, vol. 83, no. 11, Article ID 2265, 3 pages, 2003.
- [37] S. Dong, J. F. Li, and D. Viehland, "Giant magneto-electric effect in laminate composites," *IEEE Transactions on Ultrasonics, Ferroelectrics, and Frequency Control*, vol. 50, no. 10, pp. 1236–1239, 2003.
- [38] G. Srinivasan, E. T. Rasmussen, J. Gallegos, R. Srinivasan, Y. I. Bokhan, and V. M. Laletin, "Magnetoelectric bilayer and multilayer structures of magnetostrictive and piezoelectric oxides," *Physical Review B*, vol. 64, no. 21, Article ID 214408, 6 pages, 2001.
- [39] G. Srinivasan, E. T. Rasmussen, and R. Hayes, "Magnetoelectric effects in ferrite-lead zirconate titanate layered composites: the influence of zinc substitution in ferrites," *Physical Review B*, vol. 67, no. 1, Article ID 014418, 11 pages, 2003.
- [40] V. M. Laletin, N. Paddubnaya, G. Srinivasan et al., "Frequency and field dependence of magnetoelectric interactions in layered ferromagnetic transition metal-piezoelectric lead zirconate titanate," *Applied Physics Letters*, vol. 87, no. 22, Article ID 222507, 3 pages, 2005.
- [41] N. Cai, C.-W. Nan, J. Zhai, and Y. Lin, "Large high-frequency magnetoelectric response in laminated composites of piezoelectric ceramics, rare-earth iron alloys and polymer," *Applied Physics Letters*, vol. 84, no. 18, Article ID 3516, 3 pages, 2004.
- [42] S. Dong, J. Zhai, J. Li, and D. Viehland, "Near-ideal magnetoelectricity in high-permeability magnetostrictive/ piezofiber laminates with a (2-1) connectivity," *Applied Physics Letters*, vol. 89, no. 25, Article ID 252904, 3 pages, 2006.
- [43] S. Dong, J. F. Li, and D. Viehland, "A longitudinal-longitudinal mode TERFENOL-D/Pb(Mg_{1/3}Nb_{2/3})O₃-PbTiO₃ laminate composite," *Applied Physics Letters*, vol. 85, no. 22, Article ID 5305, 2 pages, 2004.
- [44] J.-P. Zhou, H. He, Z. Shi, and C.-W. Nan, "Magnetoelectric CoFe₂O₄/Pb(Zr_{0.52}Ti_{0.48})O₃ double-layer thin film prepared

- by pulsed-laser deposition,” *Applied Physics Letters*, vol. 88, no. 1, Article ID 013111, 3 pages, 2006.
- [45] C. Deng, Y. Zhang, J. Ma, Y. Lin, and C.-W. Nan, “Magnetic-electric properties of epitaxial multiferroic NiFe₂O₄-BaTiO₃ heterostructure,” *Journal of Applied Physics*, vol. 102, no. 7, Article ID 074114, 5 pages, 2007.
- [46] H.-C. He, J.-P. Zhou, J. Wang, and C.-W. Nan, “Multiferroic Pb(Zr_{0.52}Ti_{0.48})O₃-Co_{0.9}Zn_{0.1}Fe₂O₄ bilayer thin films via a solution processing,” *Applied Physics Letters*, vol. 89, no. 5, Article ID 052904, 3 pages, 2006.
- [47] H. Ryu, P. Murugavel, J. H. Lee et al., “Magnetoelectric effects of nanoparticulate Pb(Zr_{0.52}Ti_{0.48})O₃-NiFe₂O₄ composite films,” *Applied Physics Letters*, vol. 89, no. 10, Article ID 102907, 3 pages, 2006.
- [48] Y. G. Ma, W. N. Cheng, M. Ning, and C. K. Ong, “Magnetoelectric effect in epitaxial Pb(Zr_{0.52}Ti_{0.48})O₃/La_{0.7}Sr_{0.3}MnO₃ composite thin film,” *Applied Physics Letters*, vol. 90, no. 15, Article ID 152911, 3 pages, 2007.
- [49] S. Q. Ren, L. Q. Weng, S.-H. Song, F. Li, J. G. Wan, and M. Zeng, “BaTiO₃/CoFe₂O₄ particulate composites with large high frequency magnetoelectric response,” *Journal of Materials Science*, vol. 40, no. 16, pp. 4375–4378, 2005.
- [50] W. E. Kramer, R. H. Hopkins, and M. R. Daniel, “Growth of oxide in situ composites: the systems lithium ferrite-lithium niobate, lithium ferrite-lithium tantalate, and nickel ferrite-barium titanate,” *Journal of Materials Science*, vol. 12, no. 2, pp. 409–414, 1977.
- [51] B. S. Kang, D. G. Choi, and S. K. Choi, “Effects of grain size on pyroelectric and dielectric properties of Pb_{0.9}La_{0.1}TiO₃ ceramic,” *Journal of the Korean Physical Society*, vol. 32, supplement 1, pp. S232–S234, 1998.
- [52] H. T. Martirena and J. C. Burfoot, “Grain-size effects on properties of some ferroelectric ceramics,” *Journal of Physics C*, vol. 7, no. 17, Article ID 3182, 1974.
- [53] S. Choudhury, Y. L. Li, C. Krill, and L. Q. Chen, “Effect of grain orientation and grain size on ferroelectric domain switching and evolution: phase field simulations,” *Acta Materialia*, vol. 55, no. 4, pp. 1415–1426, 2007.
- [54] H. M. Duiker and P. D. Beale, “Grain-size effects in ferroelectric switching,” *Physical Review B*, vol. 41, no. 1, pp. 490–495, 1990.
- [55] V. Sundar, N. Kim, C. A. Randall, R. Yimnirun, and R. E. Newnham, “The effect of doping and grain size on electrostriction in PbZr_{0.52}TiO_{0.48}O₃,” in *Proceedings of the 10th IEEE International Symposium on Applications of Ferroelectrics (ISAF '96)*, vol. 2, pp. 935–938, August 1996.
- [56] C. J. Lu, S. B. Ren, H. M. Shen, J. S. Liu, and Y. N. Wang, “The effect of grain size on domain structure in unsupported PbTiO₃ thin films,” *Journal of Physics Condensed Matter*, vol. 8, no. 42, pp. 8011–8016, 1996.
- [57] C. Sakaki, B. L. Newalkar, S. Komarneni, and K. Uchino, “Grain size dependence of high power piezoelectric characteristics in Nb doped lead zirconate titanate oxide ceramics,” *Japanese Journal of Applied Physics 1*, vol. 40, no. 12, pp. 6907–6910, 2001.
- [58] T. Takeuchi, T. Tani, and Y. Saito, “Piezoelectric properties of bismuth layer-structured ferroelectric ceramics with a preferred orientation processed by the reactive templated grain growth method,” *Japanese Journal of Applied Physics 1*, vol. 38, no. 9, pp. 5553–5556, 1999.
- [59] S. Kwon, E. M. Sabolsky, G. L. Messing, and S. Trolier-McKinstry, “High strain,(001) textured 0.675Pb(Mg_{1/3}Nb_{2/3})O₃-0.325PbTiO₃ ceramics:templated grain growth and piezoelectric properties,” *Journal of the American Ceramic Society*, vol. 88, no. 2, pp. 312–317, 2005.
- [60] J. L. Jones, S. C. Vogel, E. B. Slamovich, and K. J. Bowman, “Quantifying texture in ferroelectric bismuth titanate ceramics,” *Scripta Materialia*, vol. 51, no. 12, pp. 1123–1127, 2004.
- [61] R. A. Islam and S. Priya, “Enhanced magnetoelectric effect in (1 - x) Pb(Zr_{0.52}Ti_{0.48})O₃-xNiFe_{1.9}Mn_{0.1}O₄ particulate composites—electrical and magnetic properties,” *Integrated Ferroelectrics*, vol. 82, no. 1, pp. 1–24, 2006.
- [62] R. A. Islam and S. Priya, “Annealing and aging effect in 0.95 Pb(Zr_{0.52}Ti_{0.48})O₃-0.05 NiFe_{1.9}Mn_{0.1}O₄ particulate magnetoelectric composites,” *Japanese Journal of Applied Physics 2*, vol. 45, no. 4–7, pp. L128–L131, 2006.
- [63] R. A. Islam and S. Priya, “Synthesis of high magnetoelectric coefficient composites using annealing and aging route,” *International Journal of Applied Ceramic Technology*, vol. 3, no. 5, pp. 353–363, 2006.
- [64] H. W. Kim, S. Priya, K. Uchino, and R. E. Newnham, “Piezoelectric energy harvesting under high pre-stressed cyclic vibrations,” *Journal of Electroceramics*, vol. 15, no. 1, pp. 27–34, 2005.
- [65] R. A. Islam and S. Priya, “Realization of high-energy density polycrystalline piezoelectric ceramics,” *Applied Physics Letters*, vol. 88, no. 3, Article ID 032903, 3 pages, 2006.
- [66] S. Priya, Ph.D. dissertation, Pennsylvania State University, University Park, Pa, USA, 2003.
- [67] S. Priya and K. Uchino, “Dielectric and piezoelectric properties of the Mn-substituted Pb(Zn_{1/3}Nb_{2/3})O₃-PbTiO₃ single crystal,” *Journal of Applied Physics*, vol. 91, no. 7, Article ID 4515, 6 pages, 2002.
- [68] S. Priya, K. Uchino, and D. Viehland, “Crystal growth and piezoelectric properties of Mn-substituted Pb(Zn_{1/3}Nb_{2/3})O₃ single crystal,” *Japanese Journal of Applied Physics 2*, vol. 40, no. 10, pp. L1044–L1047, 2001.
- [69] S. Priya, K. Uchino, and D. Viehland, “Fe-substituted 0.92 Pb(Zn_{1/3}Nb_{2/3})O₃-0.08PbTiO₃ single crystals: a “hard” piezocrystal,” *Applied Physics Letters*, vol. 81, no. 13, Article ID 2430, 3 pages, 2002.
- [70] S. Priya and K. Uchino, “High power resonance characteristics and dielectric properties of co-substituted 0.92Pb(Zn_{1/3}Nb_{2/3})O₃-0.08PbTiO₃ single crystal,” *Japanese Journal of Applied Physics 1*, vol. 42, no. 2, pp. 531–534, 2003.
- [71] S. Priya, J. Ryu, K. Uchino, C. W. Ahn, and S. Nahm, “Induction of combinatory characteristics by relaxor modification of Pb(Zr_{0.5}Ti_{0.5})O₃,” *Applied Physics Letters*, vol. 83, no. 24, Article ID 5020, 3 pages, 2003.
- [72] C. A. Randall, N. Kim, J. P. Kucera, W. Cao, and T. R. Shrout, “Intrinsic and extrinsic size effects in fine-grained morphotropic-phase-boundary lead zirconate titanate ceramics,” *Journal of the American Ceramic Society*, vol. 81, no. 3, pp. 677–688, 1998.
- [73] K. I. Kobayashi, H. Morinaga, T. Araki, Y. Naka, and T. Oomura, “Low-loss Ni-Zn-Cu ferrite for deflection yoke,” *Journal of Magnetism and Magnetic Materials*, vol. 104–107, part 1, pp. 413–414, 1992.
- [74] I. Z. Rahman, T. T. Ahmed, and L. Powell, “Magnetic and physical characterization of nano granular Ni-Zn-Cu based ferrite powders,” *Journal of Metastable and Nanocrystalline Materials*, vol. 17, pp. 9–16, 2003.
- [75] W. C. Kim and S. J. Kim, “Magnetic properties of NiZnCu ferrite powders and thin films prepared by a sol-gel method,” *IEEE Transactions on Magnetics*, vol. 37, no. 4, pp. 2362–2365, 2001.

- [76] J. J. Shrotri, S. D. Kulkarni, C. E. Deshpande et al., "Effect of Cu substitution on the magnetic and electrical properties of Ni-Zn ferrite synthesized by soft chemical method," *Materials Chemistry and Physics*, vol. 59, no. 1, pp. 1–5, 1999.
- [77] T. T. Ahmed, I. Z. Rahman, and M. A. Rahman, "Study on the properties of the copper substituted NiZn ferrites," *Journal of Materials Processing Technology*, vol. 153-154, no. 1–3, pp. 797–803, 2004.
- [78] T. Okamura and Y. Kojima, "Ferromagnetic resonance in copper ferrite," *Physical Review*, vol. 86, no. 6, pp. 1040–1041, 1952.
- [79] R. E. Newnham, "Electroceramics," *Reports on Progress in Physics*, vol. 52, no. 2, pp. 123–156, 1989.
- [80] Z. J. Zhang, Z. L. Wang, B. C. Chakoumakos, and J. S. Yin, "Temperature dependence of cation distribution and oxidation. State in magnetic Mn-Fe ferrite nanocrystals," *Journal of the American Chemical Society*, vol. 120, no. 8, pp. 1800–1804, 1998.
- [81] R. A. Islam, D. Viehland, and S. Priya, *Journal of Materials Science Letters*, 2007.
- [82] R. A. Islam and S. Priya, *Journal of Materials Science Letters*, 2007.
- [83] R. A. Islam and S. Priya, "Magnetoelectric properties of the lead-free cofired $\text{BaTiO}_3\text{-(Ni}_{0.8}\text{Zn}_{0.2})\text{Fe}_2\text{O}_4$ bilayer composite," *Applied Physics Letters*, vol. 89, no. 15, Article ID 152911, 3 pages, 2006.
- [84] R. A. Islam, J. Jiang, S. Priya, F. Bai, and D. Viehland, "Correlation between structural deformation and magnetoelectric response in $(1-x)\text{Pb}(\text{Zr}_{0.52}\text{Ti}_{0.48})\text{O}_3\text{-xNiFe}_{1.9}\text{Mn}_{0.1}\text{O}_4$ particulate composites," *Applied Physics Letters*, vol. 91, no. 16, Article ID 162905, 3 pages, 2007.
- [85] T. Takeuchi, T. Tani, and Y. Saito, "Piezoelectric properties of bismuth layer-structured ferroelectric ceramics with a preferred orientation processed by the reactive templated grain growth method," *Japanese Journal of Applied Physics 1*, vol. 38, no. 9, pp. 5553–5556, 1999.
- [86] S. H. Hong, S. T. Trolier-McKinstry, and G. L. Messing, "Dielectric and electromechanical properties of textured niobium-doped bismuth titanate ceramics," *Journal of the American Ceramic Society*, vol. 83, no. 1, pp. 113–118, 2000.
- [87] A. Moure, L. Pardo, C. Alemany, P. Millán, and A. Castro, "Piezoelectric ceramics based on $\text{Bi}_3\text{TiNbO}_9$ from mechanochemically activated precursors," *Journal of the European Ceramic Society*, vol. 21, no. 10-11, pp. 1399–1402, 2001.
- [88] M. Allahverdi, A. Hall, R. Brennan, M. E. Ebrahimi, N. M. Hagh, and A. Safari, "An overview of rapidly prototyped piezoelectric actuators and grain-oriented ceramics," *Journal of Electroceramics*, vol. 8, no. 2, pp. 129–137, 2002.
- [89] K. Watari, B. Brahmaroutu, G. L. Messing, S. Trolier-McKinstry, and S.-C. Cheng, "Epitaxial growth of anisotropically shaped, single-crystal particles of cubic SrTiO_3 ," *Journal of Materials Research*, vol. 15, no. 4, pp. 846–849, 2000.
- [90] E. M. Sabolsky, S. Trolier-McKinstry, and G. L. Messing, "Dielectric and piezoelectric properties of $\langle 001 \rangle$ fiber-textured $0.675\text{Pb}(\text{Mg}_{1/3}\text{Nb}_{2/3})\text{O}_3\text{-}0.325\text{PbTiO}_3$ ceramics," *Journal of Applied Physics*, vol. 93, no. 7, Article ID 4072, 9 pages, 2003.
- [91] J. P. Remeika, *Notes*, vol. 76, p. 940, 1953.
- [92] Y. S. Koo, T. Bonaedy, K. D. Sung et al., "Magnetodielectric coupling in core/shell $\text{BaTiO}_3/\gamma\text{-Fe}_2\text{O}_3$ nanoparticles," *Applied Physics Letters*, vol. 91, no. 21, Article ID 212903, 3 pages, 2007.
- [93] G. Rowlands, "The variation of coercivity with particle size," *Journal of Physics D*, vol. 9, no. 8, Article ID 1267, 1976.
- [94] K. Uestuener, M. Katter, and W. Rodewald, "Dependence of the mean grain size and coercivity of sintered Nd-Fe-B magnets on the initial powder particle size," *IEEE Transactions on Magnetics*, vol. 42, no. 10, Article ID 2897, 2006.
- [95] S. Priya, R. Islam, S. Dong, and D. Viehland, "Recent advancements in magnetoelectric particulate and laminate composites," *Journal of Electroceramics*, vol. 19, no. 1, pp. 147–164, 2007.